universität wien

MASTER'S THESIS

Effects of microbial activity and silicate alteration on porefluid alkalinity and carbonate diagenesis in a deep methanogenic zone at the Peru Margin (ODP Site 1230)

submitted by

Gerhard Herda, BSc

in partial fulfilment of the requirements for the degree of

Master of Science (MSc)

Vienna 2017

degree programme code as it appears on the student record sheet:	A 066 815
degree programme as it appears on the student record sheet:	Earthsciences
Supervisor:	Dr. Patrick Meister

Abstract

The formation of early diagenetic carbonates is of interest as it affects the geological record and preserves and/or alters geochemical signatures indicative of past environments and life. The factors affecting carbonate diagenesis are diverse, but largely depend on processes increasing carbonate (CO_3^{2-}) concentration and therefore the saturation state of the porefluid with respect to different carbonate minerals. An important factor for carbonate precipitation is alkalinity production by microbial activity, such as sulphate reduction (SR) and anaerobic oxidation of methane (AOM). In contrast, production of CO_2 by fermentative processes, such as methanogenesis, cause acidification of the porefluid and counteract the formation of carbonates. Partial dissolution (weathering) of silicates during early diagenesis seems to have an influence on fluid alkalinity during burial diagenesis, and it has been suggested that the additional alkalinity from clay mineral alteration may drive carbonate precipitation even in strongly methanogenic zones. These processes seem to have great influence on carbonate diagenesis but are not fully understood yet.

In this study, the share of alkalinity produced by microbial activity to 150 mmol/l measured alkalinity at ODP Site 1230 is quantified with a diffusion model and the possibility of additional porewater alkalinity increase through (clay) mineral equilibrium calculations is evaluated.

With up to 115 mmol/l alkalinity in porewater (calculated by fitting the results of a reaction transport model with measured ammonium concentrations) exlusively produced through microbial activity, calcite is slightly oversaturated between 30 and 140 mbsf at ODP Site 1230, despite a contribution of up to 240 mmol/l of dissolved CO_2. Apart from previously described shallow dolomite layers (*Meister et al., 2011*), bulk XRD shows the occurrence of calcite between 60 and 140 mbsf which is deep in the zone of methanogenesis between 60 and 140 mbsf: this confirms the prediction of the model.

For calculations of mineral reactions the computer program PHREEQC, available from the United State Geological Survey, was used. Three out of 48 thermodynamically possible combinations of minerals, K-feldspar, illite, kaolinite, montmorillonite, chlorite, calcite and SiO_2 (opal A) with input-parameter from the diffusion-model, reproduce measured [Ca^{2+}], [Mg^{2+}], DIC and alkalinity of the porewater of ODP Site 1230 best. Single calcite + SiO_2(a) equilibrium (scenario 6) with initial solution leads to a decrease of alkalinity but fits well [Ca^{2+}] of the profile. Chlorite + SiO_2(a) (scenario 5) reaction increases alkalinity by ≈ 45 mmol/l but does not include any carbonate phase. The combination of both reactions (scenario

21), respectively the equilibrium of chlorite, calcite and SiO_2(a) with the initial solution, comes closest measured [Ca^{2+}], [Mg^{2+}], DIC and alkalinity of the porewater of ODP Site 1230. Due to simulating mineral reaction through congruent dissolution, chlorite may stand vicarious for any reactive clay mineral.

One insight gained from this study is that incongruent dissolution of clay mineral has a major capacity to drive carbonate diagenesis. However, the processes are largely inhibited or slow. Results demonstrate that clay mineral alteration processes are far away from equilibrium. Overcoming these kinetic barriers would be essential for first concepts of CO_2 storage reservoirs in eligible geological units (*Fischer et al., 2010; Kasina et al., 2014*). Carbonate precipitation could be induced to permanently trap and store CO_2 in the form of carbonate rock. Regarding questions of chemical equilibria, geochemical modelling is an adequate and important method to get an idea of very complex problems (e.g *Boudreau, 1997*).

Table of content

1. Introduction

Carbonate diagenesis influences cementation of the sediment and contributes to the formation and preservation of geological archives. Important factors controlling carbonate dissolution or precipitation are (1) the saturation state of carbonate phases in a solution (e.g seawater or porewater) and (2) the overcoming of the kinetic inhibition. Various processes like temperature- and pressure-change but also microbial alkalinity production lead to oversaturation of carbonates and are not fully understood. While sulphate reduction (SR) and anaerobic oxidation of methane (AOM) produce high amounts of alkalinity (through HS^- and HCO_3^- release) in the shallower sediment, the CO_2 release of the deeper methanogenic zone should undersaturate carbonates. However, diagenetic carbonates with strong methanogenic $\delta^{13}C$ signature are descried in ODP Site 1230 located at the Peru margin (*Meister et al., 2011*).

This Peruvian continental slope is dominated by intensive coastal upwelling which enables very high primary productivity. Resulting low oxygen in the water column favours preservation and sedimentation of TOC (*Arndt et al., 2013*). Strong microbial activity within the anoxic sediment affects the porewater chemistry by oxidizing organic substrates with available oxidants (*Fröhlich et al., 1979)*. Table 1 shows typical redox-reactions occurring in the sequence of decreasing Gibbs free energy (G). The Gibbs free energy and availability of electron acceptors control which reactions take place in the sediment. The changing of Redox-conditions with depth leads to a zonation characterised by distinct species measurable in the porewater.

Table 1: Simplified redox-processes in a stratified sediment (*Konhauser 2006; Schmidt et al. 2011*).

Reaction	**Gibbs free Energy (Δ_rG_0)**
$CH_3COO^- + O_2 \rightarrow H_2O + CO_2 + OH^-$	-854 kJ/reaction
$CH_3COO^- + 1.6\ NO_3^- \rightarrow 2\ CO_2 + 0.8\ N_2 + 2.6\ OH^- + 0.2\ H_2O$	-801 kJ/reaction
$CH_3COO^- + 4\ MnO_2 + 3\ H_2O \rightarrow 4\ Mn^{2+} + 2\ HCO_3^- + 7\ OH^-$	-558 kJ/reaction
$CH_3COO^- + 8\ Fe(OH)_3 \rightarrow 8\ Fe^{2+} + 2\ HCO_3^- + 15\ OH^- + H_2O$	-337 kJ/reaction
$CH_3COO^- + SO_4^{2-} \rightarrow HS^- + 2\ HCO_3^-$	-48 kJ/reaction

High rates of sulphate reduction lead to a steep SO_4^{2-} gradient with depth and shallow sulphate-methane transition zones (SMTZ). If all electron acceptors are consumed, microbial activity can still occur through fermentation, such as acetoclastic methanogenesis:

$$CH_3COO^- + H_2O + H^+ \rightarrow CH_4 + CO_2 + H_2O \quad \textbf{Eq. (1)}$$

$$\Delta G = -31\ kJ/reaction$$

This leads to large amounts of methane and carbon dioxide (CO_2), which acidifies the porewater and decreases pH. Actually, equation 1 is only one of two kinds of methanogenesis. Another pathway of CH_4-production is autotrophic methanogenesis described with equation 2.

Hydrogen generation by fermentation:	$2\ CH_2O + 2\ H_2O \rightarrow 4\ H_2 + 2\ CO_2$
Hydrogenotrophic methanogenesis:	$CO_2 + 4\ H_2 \rightarrow CH_4 + 2\ H_2O$
Overall reaction:	**$2\ CH_2O \rightarrow CH_4 + CO_2$ Eq. (2)**

However, layers of early diagenetic dolomite were found more than 230 meters below seafloor at ODP Site 1230 (*Wehrmann et al., 2013*). A $\delta^{13}C$ value of ≈ +15‰ indicates formation deep in the zone of methanogenesis where carbonate precipitation should be inhibited or even dissolution should be favoured. Strontium-87 and oxygen-18 measured in the dolomites (*Kastner et al., 1990*) indicates an influence of upward-flowing fluids from greater depth, which may buffer the low pH from CO_2 acidification and supply Ca-ions from beneath (*Meister et al., 2011*), but the process leading to such dolomite layers is still unclear.

1.1 Alkalinity and DIC generation in methanogenic zone of Site 1230

Sulphate reduction increases alkalinity and strongly affects porewater chemistry (*Meister, 2013*). A few metres below the sediment surface of ODP Site 1230, the bioavailable sulphate is depleted and anaerobic oxidation of methane (AOM) is dominant. In the transition zone between sulphate reduction and methanogenesis, ascending CH_4 is oxidised by SO_4^{2-}, which produces alkalinity and dissolved inorganic carbon (DIC; Eq. (3)) (*D'Hondt et al., 2002*).

$$[DIC] = [H_2CO_3] + [HCO_3^-] + [CO_3^{2-}] \quad \textbf{Eq. (3)}$$

The lower 100 meters of the sediment profile are sulphate-free and microbial degradation of organic matter produces high amounts of methane and CO_2. The dominating microbial and abiotic processes producing alkalinity within the sediment-column (*Wallmann et al., 2008*) have different influences on the porewater chemistry which are summarised in table 2:

Table 2: Influence on alkalinity and DIC from main microbial processes and carbonate precipitation

	Reaction	Alkalinity	DIC
Sulphate Reduction (SR)	$SO_4 + 2\ CH_2O^* \rightarrow HS^- + 2\ HCO_3^- + H^+$	+2	+2
Ammonium release	$NH_3 + H^+ \rightarrow NH_4^+$	+1	0
Anaerobic oxidation of methane (AOM)	$SO_4 + CH_4 \rightarrow HS^- + HCO_3^- + H_2O$	+2	+1
Methanogenesis	$2\ CH_2O^* \rightarrow CH_4 + CO_2$	0	+1
Carbonate precipitation	$Ca^{2+} + HCO_3^- \rightarrow CaCO_3 + H^+$	-1	-1

*CH_2O stands for generalised organic matter

In addition, a high value of 150 mmol/l total alkalinity measured in porewater of ODP Site 1230 suggests the occurrence of silicate alteration processes (*Wallmann, 2008; Meister et al., 2007*). In zones of natural CO_2 production, all minerals (silicates, carbonates as well as clay minerals) adapt under different chemical conditions towards more stable states during burial. These processes also have the potential to buffer strong acidification. Alternatively and/or additionally upward-flowing fluids in anoxic marine sediments are discussed (*Wallmann et al., 2008*).

By convention, silicate weathering/alteration is a process of incongruent dissolution which consumes CO_2 to form secondary major-cation depleted minerals (*Amiotte Suchet et al. 2003; Colbourn et al. 2015),* while the term reverse weathering describes the opposite related to the effect on CO_2 and cations inclusively dissolved SiO_2 (*Wallmann et al., 2008*). The following equation from *Scholz et al. (2013)* shows the simplified alteration reactions from (volcanic) detritus and their contribution to alkalinity through HCO_3^- production or consumption:

Kaolinite formation by generalised silicate alteration:

$$[(K,Na)_2O;\ MgO;\ CaO;\ Al_2O_3;\ SiO_2] + H_4SiO_4 + 6\ CO_2 + 3\ H_2O \rightarrow$$
$$Al_2Si_2O_5(OH)_4 + K^+ + Na^+ + Mg^{2+} + Ca^{2+} + 6\ HCO_3^- \quad \textbf{Eq. (4)}$$

Reverse weathering from *Wallmann et al., 2008*:

$$\text{(Biogenic) Opal + metal hydroxides + dissolved cations + } HCO_3^- \rightarrow$$
$$\text{clay minerals + } CO_2 \quad \textbf{Eq. (5)}$$

Submarine alteration processes can buffer low pH in deep marine sediments and can be an alternative source of alkalinity in zones of strong methanogenesis (*Aloisi et al., 2004*). This process may also induce carbonate precipitation, but it is still poorly understood.

However, alteration of sediments under high pCO_2 is not only an academic question but also a practical one. To decrease greenhouse gases, especially CO_2, in the atmosphere first concepts of storage in suitable porous rock-reservoirs are discussed and tested (*Fischer et al., 2010; Wandrey et al., 2011; Kasina et al., 2014; Fischer et al., 2014*).

To advance this method a better understanding of rock-fluid interaction under acidic conditions is necessary and the investigation of organic carbon-rich deep marine sediments from ODP Site 1230 provides three major advantages: (1) Due to natural CO_2 production no additional artificial acidification is needed; (2) the sediment system is up to Eocene age, so reactions occurred over geological timescales respectively mineral phases are expected to be in equilibrium and (3) the high DIC conditions allows us to extrapolate the behaviour of CO_2 reservoirs into the future.

1.2 Goal of the study

Especially for poor accessible deep-marine sediment systems, geochemical modelling is an adequate method to deal with complex problems. Generalisations of biogeochemical processes in nature may be useful to improve the understanding of diagenetic processes, such as clay mineral formation and silicate weathering, in a systematic way (*Stumm and Morgan, 1996; Arning et al., 2012*). In this study, carbonate genesis is simulated under strong methanogenic conditions and the influence of deep marine silicate alteration in ODP Leg 201 Site 1230 (*Initial Report ODP Leg 201 Site 1230, D'Hondt et al., 2003*).

In general, the ammonium concentration of porewater, alkalinity and DIC are stoichiometrically coupled through the N/C-ratio (Redfield Ratio). So a reaction transport model was calculated which fits measured $[NH_4^+]$ to determine the microbial alkalinity and DIC production.

In a next step, PHREEQC (U.S. Geological Survey; *Parkhurst and Appelo, 1999*) was used for speciation, calculation of saturation states and mineral reactions under in situ conditions at Site 1230. To simplify the model cation exchange-effects are not considered, so mineral dissolution takes place as congruent dissolution. As input-parameters for speciation calculations average cation concentration of seawater together with alkalinity and DIC from RT-model (table 6) was taken. 48 possible equilibrium reactions (respectively scenarios) of

feldspar, illite kaolinite, montmorillonite, chlorite, and calcite + SiO_2(a) were calculated and compared to identify the combination which produces alkalinity and fits best measured porewater chemistry of Site 1230. Mineral precipitation leads to cation depletion of the initial solution while dissolution reactions have the opposite effect.

Several studies showed that authigenic clay mineral formation in such anoxic marine sediments occurs both rapid (days to months) and over geological timescale (*Michalopoulos and Aller, 1995; Parkes et al., 2005*). However, in this study a pressure depending model, under near equilibrium conditions and a high solid/fluid ratio of characteristic sediments and interstitial fluids was generated in order to reproduce measured alkalinity and porewater chemistry at ODP Site 1230.

The reconstruction of microbial processes (RT-model) and mineral reactions (equilibrium model) through comparison of calculated results with measured porewater chemistry provides an explanation of up to 150 mmol/l alkalinity in porewater of Site 1230. Showing the possibility of carbonate supersaturation and alkalinity increase through clay mineral equilibrium will contribute to a better understanding of deep marine alteration processes and carbonate diagenesis.

2. Geological Setting

Regional geology along the Peru-Chile margin is dominated by the eastern Pacific plate subducting underneath the South American plate. Offshore Peru, the continental margin shows an extensive accretionary complex with overlying sediments of Eocene to Holocene age. The morphology of the continental margin (figure 1) shows three wide terraces on the upper, middle and lower slope with sediment-filled basins beneath (*ODP Initial Report Leg 112*). Normal faulted ridges commonly form the barriers between these basins (*Thornburg, 1985*), while the lower slope within the accretionary prism is disrupted by thrust faults (*Hussong and Wipperman, 1981; Hussong et al., 1985*). A subsidence rate between 275 and 500 m/Ma was calculated with benthic foraminifera assemblages for the upper slope Lima Basin (*Kulm, et al., 1981; Kulm, et al., 1984*).

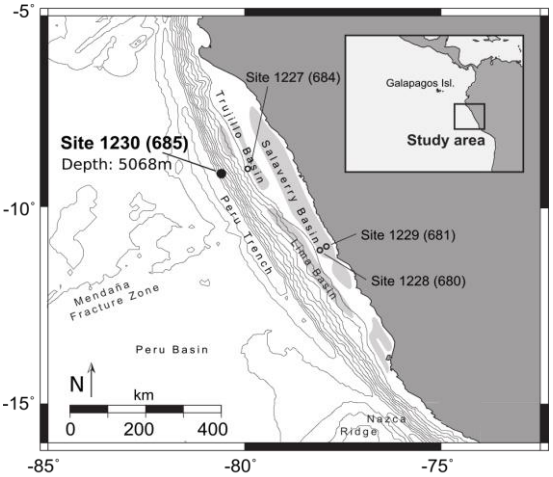

Figure 1: Map of the eastern Pacific/Peru margin showing the location of International Ocean Drilling Program (ODP) Leg 201 Site 1230 which is a re-drilled from ODP Leg 112 Site 685 (modified from *Meister et al. 2011*).

Site 1230 was drilled during Ocean Drilling Program (ODP) Leg 201 at the lower slope of the Peru margin. It is a re-drilled site from ODP Leg 112 Site 685 in a water depth of 5086 m. The depositional environment of the Eocene sediments at the bottom of the sedimentary column was a broad continental shelf with a shallow water depth. The Oligocene unit was eroded and forms a hiatus between Eocene and younger sediments. The biostratigraphically derived sedimentation rate from Site 1230 was estimated with average 130 m/Ma (*ODP Initial Report Leg 112*).

The dominant lithology is mud-rich diatomaceous sediment with a high content of organic carbon and various content of siliciclastic material. The sequence itself is characterised by alternating layers of diatom-ooze and dark-green clay (*Prokopenko et al., 2006*) and sediment structures are dominated by downslope transport from the shelf. Except several dolomite layers at depths below 230 mbsf, the site has no authigenic carbonates (calcite and dolomite) and phosphates. From 9 to 30 mbsf the sulphate concentration continuously decreases while methane concentration increase. Below this sulphate/methane transition zone (SMTZ) gas hydrates are present at 14 and 82 mbsf (*D'Hondt, Jørgensen, Miller, et al. 2003*). Especially in shallow depth of the sediment, high-angle and centimetre-scaled normal faults were observed (*D'Hondt et al., 2003*).

3. Material and methods

3.1 Sampling

Sediment samples from Site 1230 were provided by ODP, the Texan A&M University, and came from different depths up to 254.15 mbsf (metres below seafloor). All data were measured on board from drilling hole A. Selection criteria was (1) a regular distribution over the whole profile and (2) undisturbed occurrence of the core material from APC (advanced piston coring). Table 3 shows the description and origin of the untreated samples.

Table 3: Description of analysed samples of ODP Site 1230

Leg	Site	Hole	Core	Section	Depth (mbsf)	Abbreviation	Description
201	1230	A	2	2	6.30	2H-2W	dark green to black, uncemented clay
201	1230	A	3	1	14.30	3H-1W_1*	dark green to black, uncemented clay
201	1230	A	3	1	14.30	3H-1W_2*	dark green to black, uncemented clay
201	1230	A	3	6	21.80	3H-6W*	dark green, uncemented clay
201	1230	A	8	3	57.30	8H-3W	dark green, uncemented clay
201	1230	A	10	1	70.30	10H-1W*	dark green to black, uncemented clay
201	1230	A	11	5	85.80	11H-5W*	dark green to black, uncemented clay
201	1230	A	13	5	104.80	13H-5W*	dark green, uncemented clay
201	1230	A	15	7	125.54	15H-7W	dark green, uncemented clay
201	1230	A	18	CC	143.50	18H-CCW	dark green to black, uncemented clay
201	1230	A	22	1	168.30	22H-1W*	dark green, uncemented clay
201	1230	A	35	1	245.00	35X-1W	dark ochre, uncemented clay
201	1230	A	38	CC	254.15	38X-CCW	dark ochre, uncemented clay

* < 2μ grain size fraction was analysed

3.2 Bulk and clay mineralogy

For bulk mineralogical analysis the sediment samples were milled and analysed by X-ray diffraction (XRD) with a Panalytical X'Pert PRO diffractometer (Cu-K_α radiation, 40 kV, 40 mA, step size 0.0167, 5 s per step). The samples were loaded in the sample holders as powder.

For specific XRD-analysis a clay mineral separation of 7 non-milled sediment samples was done. First the organic content of the sediment was eliminated by oxidation with a 1:1 mixture of H_2O_2 and H_2O. To stop the reaction H_2O_2 was strongly diluted with deionised H_2O after 11 days. By 24 ½ hour sedimentation in an Atterberg-cylinder the <2 μm grain size fraction was separated (*Engelhardt et al., 1974; Gaucher et al., 2004*). Inhomogeneous cation-occupancy within the inter layers and different hydration states of clay minerals generally leads to 2 Theta angles (2θ) peaks which are difficult to identify. Thus, 50 mg separated clay mineral samples were saturated with 50 ml of KCl or $MgCl_2$ to get 1 mg/ml suspension to get homogeneous broadening-states of the inter layer. After centrifuging the samples for 5 minutes at 1500 runs per min. (rpm), spared Mg-solution was replaced by deionised H_2O. To differentiate smectite and vermiculite, Mg-rich samples were additional saturated with Mg-glycerine (MgGly) and K-ethyleneglycol (KEG). Finally, to identify expandable clay minerals the sediment samples also were tempered at 550°C (*Rösler, 1981*; *Eslinger and Pevear, 1988; Jasmund and Lagaly, 1993; Moor and Raynolds, 1997*). Table 4 shows the aim of the different preparation methods used:

Table 4: Usage of preparation methods

Used sample state	Method	Usage
Separated clay mineral sample	K-saturation	Smectite, vermiculite, illite and chlorite take up K^+ and show specific peak positions
Separated clay mineral sample	Mg-sauration	Smectite, vermiculite, illite and chlorite take up Mg^{2+} and show specific peak positions
Mg-saturated sample	MgGly-saturation	Smectite-peak moves to 4,9° 2Theta (18Å) position, vermiculite remains at 8.1-7.3 2°Theta (11-12Å) position.
K-saturated sample	KEG-saturation	Smectite-peak moves to 5.1° 2Theta (17Å) position, vermiculite remains at 8.1-7.3° 2Theta (11-12Å) position.
Separated clay mineral sample	temper	To identify swellable clay minerals and kaolinite which are not stable at high temperatures

3.3 Reaction Transport Model

The main biogeochemical reactions: sulphate reduction, methanogenesis and anaerobic oxidation of methane within the sediment column change pore water chemistry with depth. Reactants get consumed and released. Products move along chemical gradients following Fick's law of diffusion. It is a one dimensional partial differential equation which predicts how diffusion changes concentration with time. The model calculates sulphate, methane, ammonium, DIC concentration and alkalinity. Equations 6 – 10 were used for reaction transport model modified from *Arndt et al. (2006, 2009)* and *Meister et al. (2013)*. Rates of production and consumption are coupled to the degradation of organic matter. A constant TOC degradation rate was estimated.

Sulphate concentration:

$$\frac{\delta[SO_4{}^{2-}]}{\delta t} = \varphi \cdot D_S \cdot \frac{\delta^2[SO_4{}^{2-}]}{\delta z^2} - \frac{s_{TOC}}{2} \cdot \frac{[SO_4{}^{2-}]}{k+[SO_4{}^{2-}]} - S_{AOM} \quad \textbf{Eq. (6)}$$

Methane concentration:

$$\frac{\delta[CH_4]}{\delta t} = \varphi \cdot D_M \cdot \frac{\delta^2[CH_4]}{\delta z^2} + \frac{s_{TOC}}{2} - s_{AOM} \quad \textbf{Eq. (7)}$$

Ammonium concentration:

$$\frac{\delta[NH_4{}^+]}{\delta t} = \varphi \cdot D_{NH4} \cdot \frac{\delta^2[NH_4{}^+]}{\delta z^2} + s_{TOC} \cdot N/C \quad \textbf{Eq. (8)}$$

Microbial alkalinity:

$$\frac{\delta[HCO_3{}^-]}{\delta t} = \varphi \cdot D_{HCO3} \frac{\delta^2[HCO_3{}^-]}{\delta z^2} + \frac{s_{TOC}}{2} \cdot \frac{[SO_4{}^{2-}]}{ks+[SO_4{}^{2-}]} + s_{TOC} \cdot N/C + 2s_{AOM} \quad \textbf{Eq. (9)}$$

Dissolved inorganic carbon:

$$\frac{\delta[DIC]}{\delta t} = \varphi \cdot D_{HCO3-} \cdot \frac{\delta^2[DIC]}{\delta z^2} + s_{TOC} + s_{AOM} \quad \textbf{Eq. (10)}$$

$[SO_4^{2-}]$,$[CH_4]$, $[NH_4^+]$, $[HCO_3^-]$ and [DIC] are the concentrations of the species, z is the depth in meter below seafloor (mbsf), φ is the porosity, D_S, D_M and D_{NH4+} are effective diffusion constants.

The influence of the TOC degradation rate was considered through s_{TOC} and s_{AOM} (related to sulphate reduction from table 2). AOM rate was simulated through a Monod Kinetics. K_s is the half saturation constant. Input-parameters such as diffusion constants and AOM-rate constant were taken from *Schulz and Zabel, 2006*. For calculation of the alkalinity-effect of ammonium release from the decay of organic matter a N/C ratio of 6.625 was assumed. Table 5 shows all input-parameters of the reaction transport model. Unknown rates of TOC-degradation were reconstructed through varying s_{TOC} until $[NH_4^+]$ of the final solution fits measured concentration of ammonium in ODP Leg 201, Site 1230. So, this is a reverse model.

3.4 Boundary conditions

As boundary condition normal seawater with 28 mmol/l sulphate, 2 mmol/l DIC and 2.1 mmol/l alkalinity was defined while ammonium and methane concentration was assumed

with 0 mmol/l. Bicarbonate contributes most to the alkalinity, so the diffusion coefficient of alkalinity was assumed as the same as for HCO_3^-. The model does not allow flux across lower domain boundary (Dirichlet boundary condition) and accounts a temperature of 10°C. All profiles were run until a steady state was reached.

Table 5: Input-parameter of the reaction transport model (RT-model)

Parameter	Symbol	Value	Unit	Parameter	Symbol	Value	Unit
Domain size	Z	150	m	***Upper boundary conditions:***			
Depth interval	dz	10	m	Sulphate in seawater	$SO_4^{2-}{}_{SW}$	28	mmol/l
Time step	dt	70	a	Methane in seawater	CH_{4SW}	0	mmol/l
Sulphate concetration	$[SO_4^{2-}]$	outcome	mmol/l	Ammonium in seawater	$NH_4^+{}_{SW}$	0	mmol/l
Methane concetration	$[CH_4]$	outcome	mmol/l	Inorg. carbon in seawater	DIC_{SW}	2	mmol/l
Ammonium concetration	$[NH_4^+]$	outcome	mmol/l	Total alkalinity in seawater	TA_{SW}	2.1	mmol/l
Alkalinity	$[HCO_3^-]$	outcome	mmol/l	***Lower boundary conditions***			
Dissolved inorg. Carbon	[DIC]	outcome	mmol/l	Sulphate		0	mmol/l
Porosity	φ	0.7	--	Methane		0	mmol/l
Rate of TOC degradation	s_{TOC}	outcome	mmol/l/a	Ammonium		0	mmol/l
AOM rate constant	s_{AOM}	1.00E-03	a^{-1}	Inorg. carbon		0	mmol/l
Half saturation constant	K_S	10	mmol/l	Total alkalinity		0	mmol/l
Redfield (C/N) ratio	C/N	6,625	--	***Initial conditions***			
Diff. const. SO_4^{2-} (10°C)	D_S	6.79E-10	m^2/s	Sulphate		0	mmol/l
Diff. const. CH_4 (10°C)	D_M	1.06E-09	m^2/s	Methane		0	mmol/l
Diff. const. HCO_3^- (10°C)	D_{HCO3-}	7.37E-10	m^2/s	Ammonium		0	mmol/l
Diff. const. NH_4^+ (10°C)	D_{NH4+}	1.29E-09	m^2/s	DIC		0	mmol/l
				Alkalinity		0	mmol/l

3.5 Speciation calculation

Speciation calculation is based on the interstitial water compositions of Site 1230 (*D'Hondt et al., 2003; Donohue et al., 2006*). The speciation calculation relates the elements in solution to aqueous species and provides the theoretical thermodynamic activity a_i (Eq. 11) (*Parkhurst and Appelo, 2013*). Increased concentration of a real solution leads to interaction of the ions which influences the solubility product. The activity is the effective concentration related to a strongly diluted, ideal solution.

$$a_i = y_i \cdot c_i \quad \textbf{Eq. (11)}$$

a_i *activity*
y_i *dimensionless correction factor (activity coefficient)*
c_i *concentration of ion i (mol/L)*

Geochemical modelling was used to show the influence of fluid compositions on the thermodynamic stability of different clay minerals. Clay mineral reactions lead to release or uptake of ions which affects the chemistry of interstitial water and further the carbonate system especially the alkalinity and pH. For calculations PHREEQC (Version 3) code provided by the U.S. Geological Survey was used. It is a computer program for speciation, inverse geochemical calculations, batch-reaction, one-dimensional and transport calculations (*Parkhurst and Appelo, 2013*). A simple high pressure model under near equilibrium conditions and a high rock/fluid ratio of characteristic minerals and fluids was generated.

WATEQ4F-database was used because it contains the most important thermodynamic parameters of the clay minerals illite, montmorillonite, kaolinite and chlorite. Compared with (extended) Debye-Hückel, the Activity coefficient equation (Eq. 12) of WATEQ4F includes ion-specific parameters (*Merkel and Planer-Friedrich, 2002*).

$$\log(y_i) = \frac{-A \cdot z_i^2 \sqrt{I}}{1 + B \cdot a_i \sqrt{I}} + b_i \cdot I \quad \textbf{Eq. (12)}$$

A, B *temperature-depending parameters*
y_i *activity coefficient*
I *ionic strength*
z_i *charge of ion I*
a_i, b_i *ion-specific parameters*

3.6 Saturation index calculation and mineral equilibration

The fundamental law of mass action results from the amount of reactants and products of a chemical reaction (Eq. 13) in equilibrium, represented by the activity a_i of the components. If forward rate equals backward rate the value of equilibrium constant (K) is reached. Deviations to the equilibrium state are expressed by the ionic activity product (IAP), which has the same form as K (Eq. 14). The saturation index (SI) is defined as ratio between the IAP and K with respect to a given solid phase (Eq. 15). Therefore, a solution is undersaturated ($K < 0$), in equilibrium ($K = 0$) or supersaturated ($K > 0$), and, accordingly, the SI indicates the possibility for mineral to be precipitated or dissolved.

$$aA + bB = cC + dD \quad \textbf{Eq. (13)}$$

$$IAP = \frac{([C]^c \cdot [D]^d)}{([A]^a \cdot [B]^b)} \quad \textbf{Eq. (14)}$$

$$SI = \log(IAP) - \log(K) \quad \textbf{Eq. (15)}$$

IAP *Ionic activity product*
SI *saturation index*
K *equilibrium constant*

For initial solution (table 6) of the numerical batch model, average concentration of major and trace elements in seawater (*Broecker and Peng, 1982; Bruland and Lohan, 2004; Marion et al., 2011*) and alkalinity and DIC from the RT-model was used. The system is characterised by low temperature and high pressure due to a reaction-depth of more than 5000 m.

Table 6: Initial solution of model

Initial solution		
Parameter	**Value**	**Unit**
Alkalinity	2.1	meq/kg water
Temperature	10	°C
Pressure	500	bar
Ca^{2+}	13	mmol/kg water
Mg^{2+}	52	mmol/kg water
K^{+}	10	mmol/kg water
Na^{+}	466	mmol/kg water
S^{6+}	28	mmol/kg water
Al^{3+}	0.05	mmol/kg water
Si^{4+}	0.05	mmol/kg water
Cl^{-}	534	mmol/kg water
DIC	2	mmol/kg water

The simulation contains K-feldspar as silicate phase, the most important clay minerals illite, kaolinite, montmorillonite and chlorite as well as calcite + SiO_2(a). Table 7 shows the chemical formula of these minerals and the dissolution/formation reaction defined in the WATEQ-database of PHREEQC-computer code.

Table 7: Dissolution equations and thermodynamic data from WATEQ-database

Mineral	Reaction (from WATEQ-database)	ΔH (kcal)	log K
K-feldspar	$KAlSi_3O_8 + 8\ H_2O \rightarrow K^+ + Al(OH)_4^- + 3\ H_4SiO_4$	30,820	-20,573
Illite	$K_{0.6}Mg_{0.25}Al_{2.3}Si_{3.5}O_{10}(OH)_2 + 11.2\ H_2O \rightarrow 0.6\ K^+ + 0.25\ Mg^{2+} + 2.3\ Al(OH)_4^- + 3.5\ H_4SiO_4 + 1.2\ H^+$	54,684	-40,267
Kaolinite	$Al_2Si_2O_5(OH)_4 + 6\ H^+ \rightarrow 2\ Al^{3+} + 2\ H_4SiO_4 + H_2O$	-35,300	7,435
Montmorillonite	$Mg_{0.165}Al_{2.33}Si_{3.67}O_{10}(OH)_2 + 12\ H_2O \rightarrow 0.165\ Mg^{2+} + 2.33\ Al(OH)_4^- + 3.67\ H_4SiO_4 + 2\ H^+$	58,373	-45,027
Chlorite	$Mg_5Al_2Si_3O_{10}(OH)_8 + 16\ H^+ \rightarrow 5\ Mg^{2+} + 2\ Al^{3+} + 3\ H_4SiO_4 + 6\ H_2O$	-155,261	71,752
Calcite	$CaCO_3 \rightarrow Ca^{2+} + CO_3^{2-}$	-2,297	-8,480
Opal A	$SiO_2 + 2\ H_2O \rightarrow H_4SiO_4$	3,340	-2,710

4. Results

4.1 Mineralogical analysis

4.1.1 Bulk mineralogy

Analysed bulk samples from ODP Site 1230 show a sediment composition with up to 5 different crystalline phases. Figures 2 and 4 show the diffractograms of all samples with the diagnostic peak positions (Fig. 2 for samples only containing silicate minerals; Fig. 3 for samples containing calcite) and hkl-indices.

With its well pronounced peak at 26.6° 2θ, quartz (SiO_2) is the most abundant mineral in all samples. Estimated peak-areas from quartz, calculated by taking the product of the maximum peak-height and the peak-width at half maximum height (*Norrish et al., 1962*), show a slight increase with depth.

Mica at 19.9° (and 35.0°) 2θ shares its peak-position with illite (see clay mineral analysis) and occurs in all samples. The peaks are small but wide compared with all other mineral peaks, and they become wider with depth. The peak at 28.0° 2θ matches best with feldspar (*Deer et al., 1963*), which is a part of a double-peak system. The second diagnostic position of this mineral phase is 22.0° which shows the presence of feldspar in all samples. Prior to the analysis, none of the samples were washed, so each one has a halite (NaCl) peak at 31.7° 2θ position.

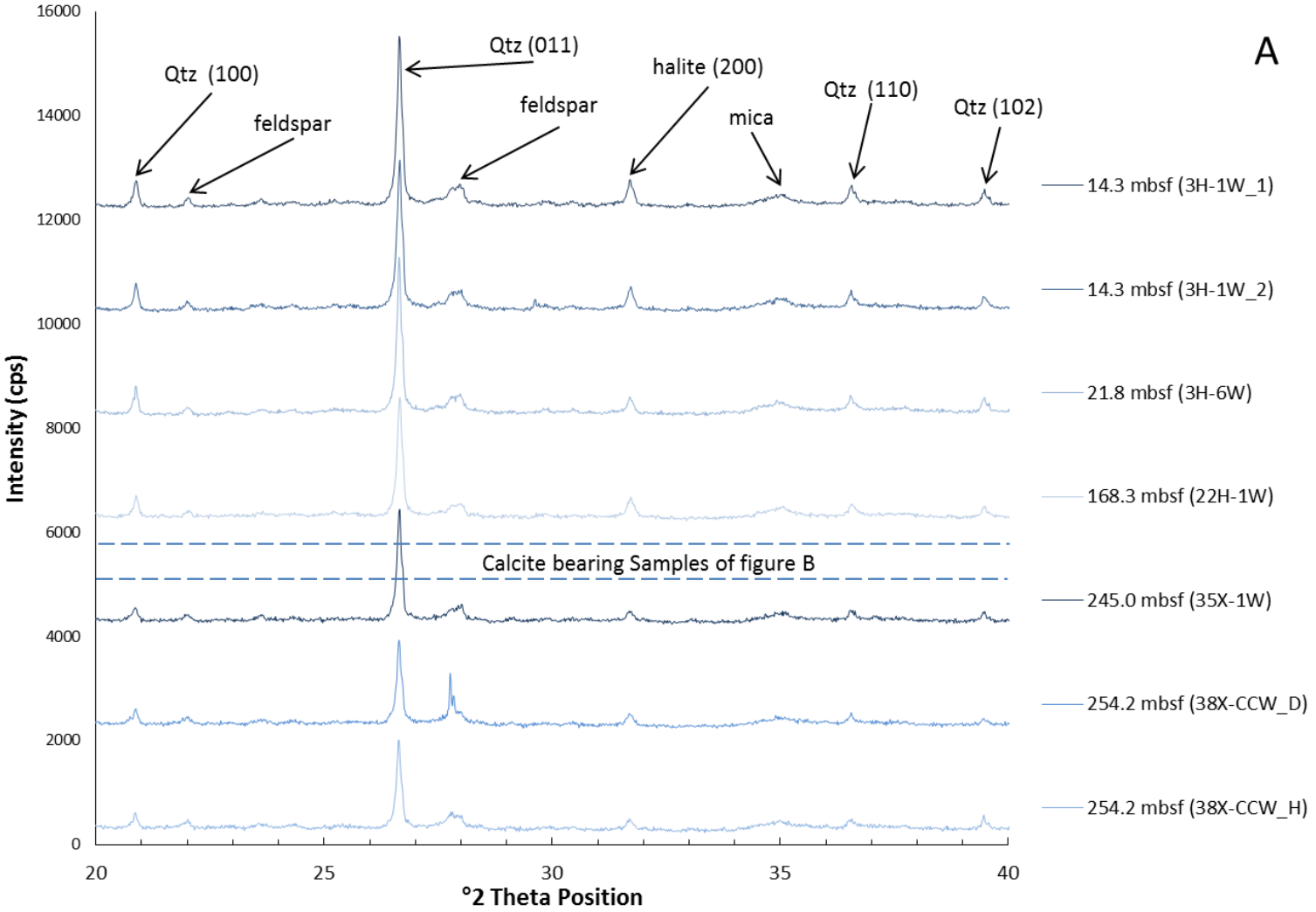
A
Qtz (100)
feldspar
Qtz (011)
feldspar
halite (200)
mica
Qtz (110)
Qtz (102)
Calcite bearing Samples of figure B
14.3 mbsf (3H-1W_1)
14.3 mbsf (3H-1W_2)
21.8 mbsf (3H-6W)
168.3 mbsf (22H-1W)
245.0 mbsf (35X-1W)
254.2 mbsf (38X-CCW_D)
254.2 mbsf (38X-CCW_H)
Intensity (cps)
°2 Theta Position
16000
14000
12000
10000
8000
6000
4000
2000
0
20
25
30
35
40

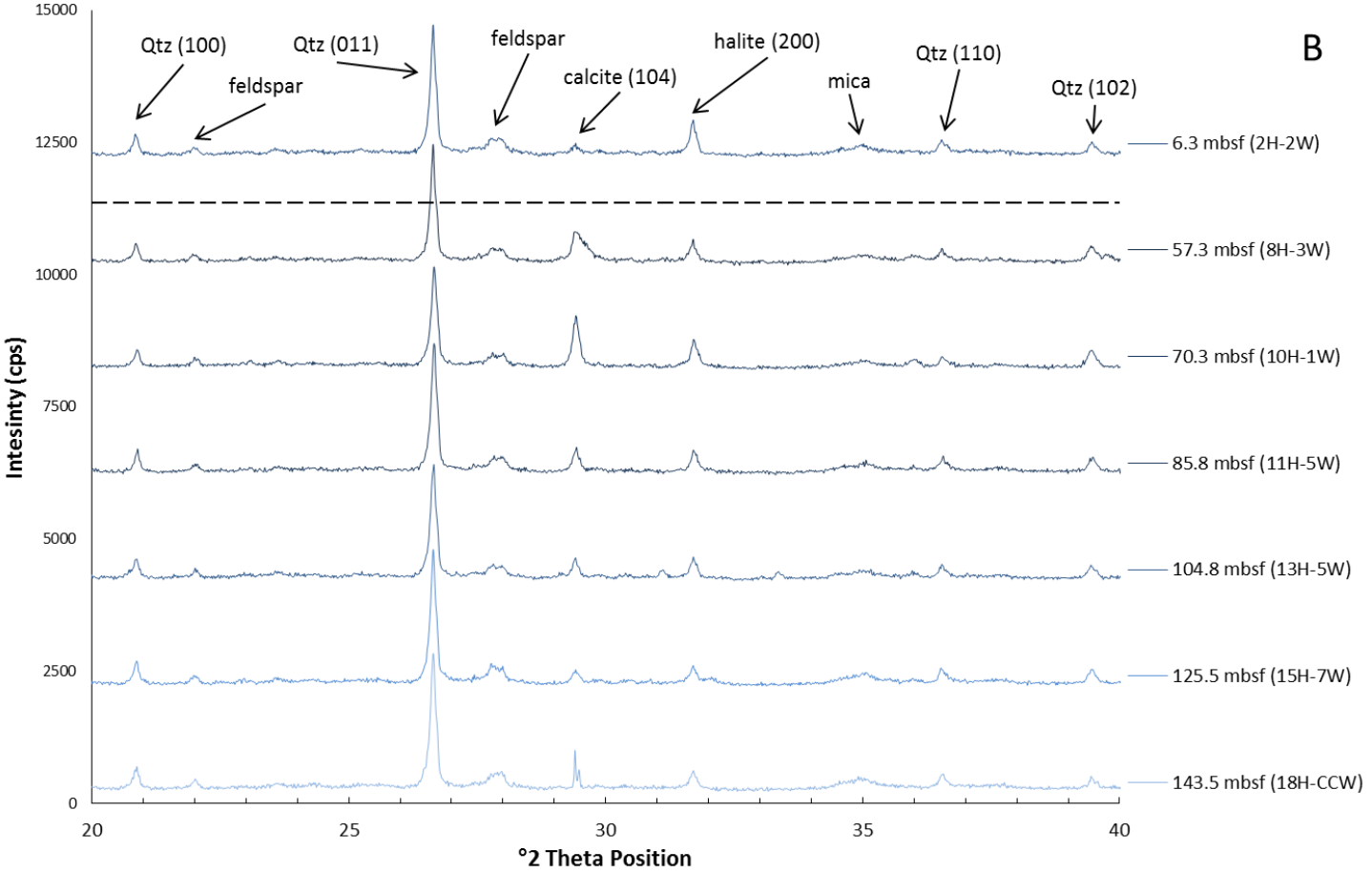

Figure 2: Bulk X-ray pattern of analysed sediment samples from ODP Site 1230. Up to five different mineral phases were identified: Quartz (Qtz) 26,6°; feldspar 28,0°; mica 35,0°; halite 31,7° and calcite 29,4°. The arrangement from top to the bottom (blue to red) follows the depth of analysed sediment. A: samples without calcite and B: samples with calcite.

Sample 2H-2W (6.30 mbsf) shows a single calcite peak. However the deeper sediments from 10H-1W (at 70.30 mbsf) to 18H-CCW (at 143.5 mbsf) show double-peaks at 2θ angles of 29.4° which indicates two different calcites with different magnesium content. Calculation of the stoichiometry using the equation of *Lumsden (1979)* indicates a magnesium-free calcite (peak 1 at 29.42° 2θ; Fig. 3) in all samples and a second magnesium-bearing calcite phase (peak 2 at ≈ 29.50° 2θ) in the samples from 57.3 to 143.5 mbsf. From 57 to 130 mbsf the Mg^{2+} content of the second calcite decreases, while the first calcite (peak 1) stays Mg-free. Table 8 shows the calculated d-spaces (in Å) and Mg-content of calcites in Site 1230.

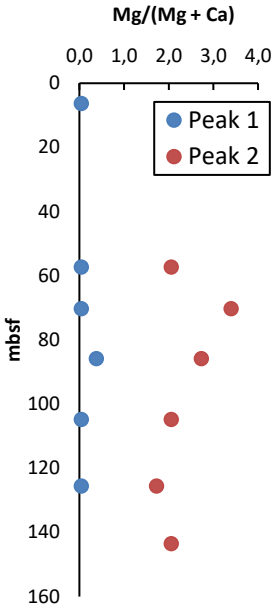

Figure 3: Mg-content of measured calcites calculated after *Lumsden 1979*.

Sample	Depth (mbsf)	d-space (Å) Peak 1	d-space (Å) Peak 2	Peak 1 (%) Mg/(Mg + Ca)	Peak 2 (%) Mg/(Mg + Ca)
2H-2W	6.3	3.0359		0.04	
8H-3W	57.3	3.0359	3.0298	0.04	2.06
10H-1W	70.3	3.0359	3.0258	0.04	3.39
11H-5W	85.8	3.0349	3.0278	0.38	2.73
13H-5W	104.8	3.0359	3.0298	0.04	2.06
15H-7W	125.54	3.0359	3.0308	0.04	1.72
18H-CCW	143.5	3.0379	3.0298	-0.63	2.06

Table 8: Mg-content of calcite calculated with the d-space from XRD-analysis. One calcite nearly is Mg-free and the Mg-content of the second one decreases from 3.4 to 1.7 %.

4.1.2 Clay mineral analysis

The <2 µm grain-size fraction was scanned from 0° to 30° 2θ. Due to the large amount of amorphous silica a strongly elevated baseline is observed between 15° and 30° 2θ. All sediments are characterised by broad and low peaks of clay mineral phases as well as the presence of quartz and feldspar. All analysed samples contain different amounts of chlorite (Chl), kaolinite (Kao), illite (Ill) and smectite-group minerals (Smc). Figure 4 shows the XRD pattern of the clay mineral separated sediment of Site 1230 with increasing depth.

All samples, except the tempered ones, show a kaolinite-chlorite double-peak system at

25° 2θ. Clearly developed peaks at 12.5° 2θ confirm the occurrence of kaolinite. High-temperature treatment (T) of the samples up to 550°C destroys kaolinite and causes a destabilisation of expandable clay minerals such as smectite-group minerals. Therefore, peaks belonging to kaolinite and the expanded minerals of the smectite-group disappear upon heating. Chlorite dehydrates and peaks at 12.6° and 25.2° 2θ positions usually disappear. But chlorite does not destabilise at high temperature, so one peak remains at 6.2° 2θ.

Due to similar crystal structure mica, illite and vermiculite share the peak at 8.9° 2θ after K^+- and Mg^{2+}- saturation. The mineral phase belonging to the portion of the 8.9° 2θ peak which is not affected by any chemical treatment (Mg^{2+}, KEG and MgGly) and high temperature is a phyllosilicate and per convention named illite (in the <2 µm grain-size fraction) or mica (in bulk samples) (*Tucker, 2017*). Vermiculite takes up ions (K^+ and Mg^{2+}) which lead to a different 8.9° 2θ peak-heigh after K^+- and Mg^{2+}-saturation. Sample 10H-1W and 11H-5W (70.3 and 85.8 mbsf) show such a peak-pattern indicating the occurrence of vermiculite. However all other samples show no or only very small vermiculite-peaks, which indicate illite as a more dominant phase.

Chlorite and smectite-group minerals share the peak at 6.2° 2θ after K^+- saturation, but only Smc takes up K-ethylene glycol (KEG) and Mg-glycerol (MgGly) which shifts its peak to 5.1° and 4.9° 2θ. This movement of the 6.2° 2θ Smc peak (in K-saturated samples) to 4.9° 2θ (in MgGly -saturated samples) is characteristic for the occurrence of smectite-group minerals (remaining peaks at 6° 2θ belong to chlorite) and occurs clearly in all samples up to 70.3 mbsf.

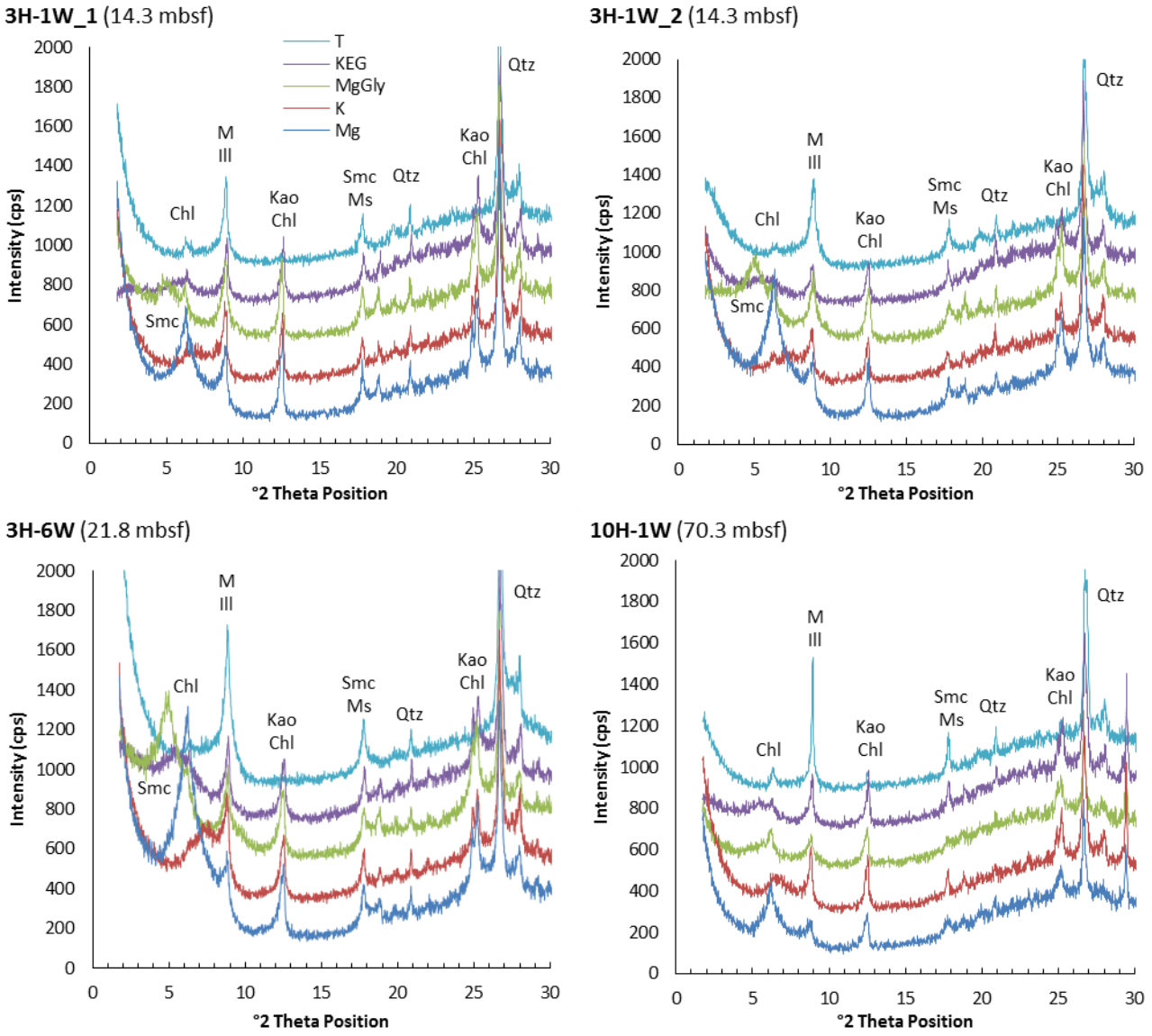
3H-1W_1 (14.3 mbsf)
T
KEG
MgGly
K
Mg
Intensity (cps)
°2 Theta Position
Chl
M
III
Kao
Chl
Smc
Ms
Qtz
Smc
3H-1W_2 (14.3 mbsf)
3H-6W (21.8 mbsf)
10H-1W (70.3 mbsf)

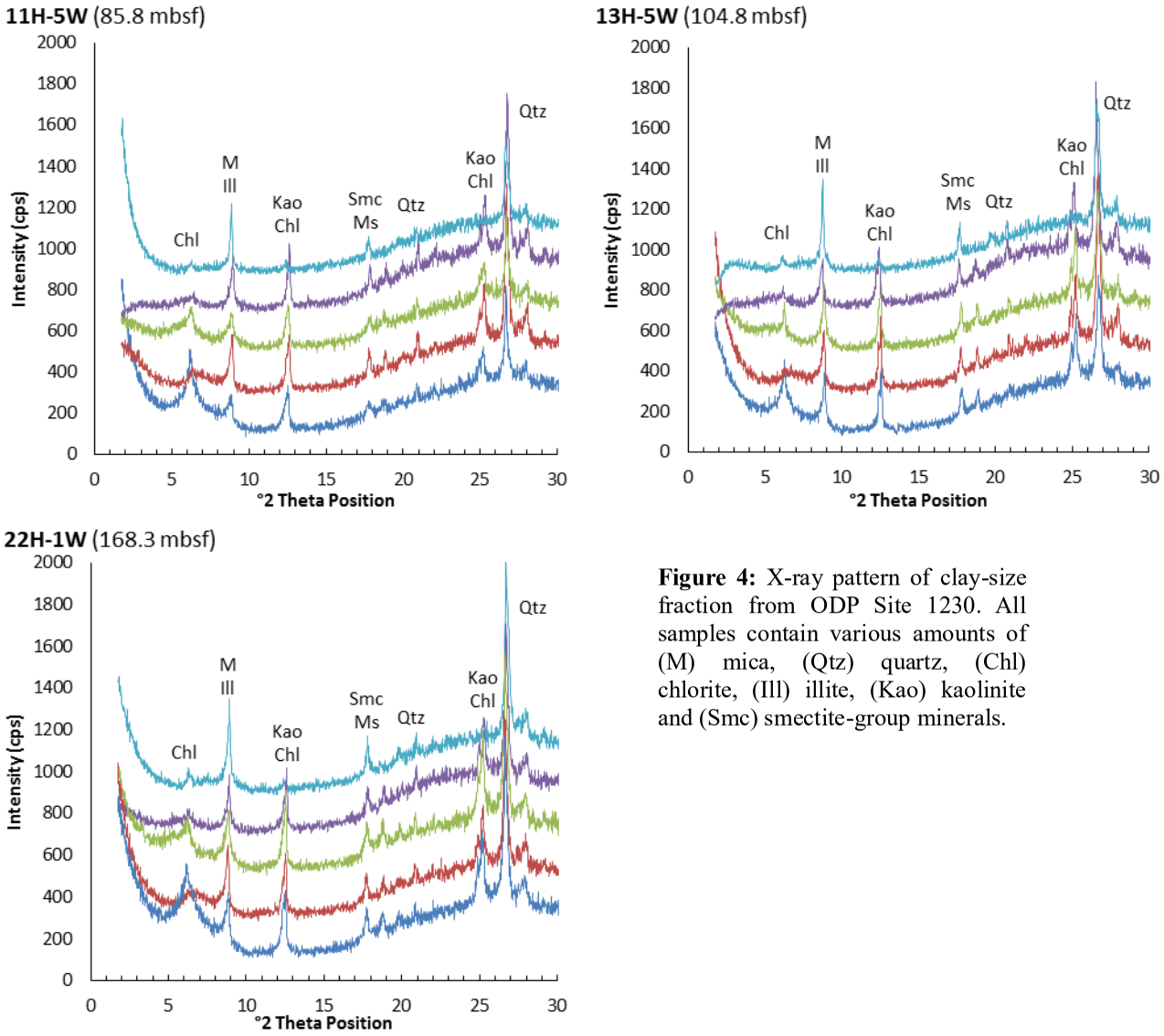

Figure 4: X-ray pattern of clay-size fraction from ODP Site 1230. All samples contain various amounts of (M) mica, (Qtz) quartz, (Chl) chlorite, (Ill) illite, (Kao) kaolinite and (Smc) smectite-group minerals.

4.2 Reaction transport model

Modelled porewater profiles reach steady state after about 11.2 Ma (Figure 5 and 6) which approximately corresponds with the oldest sediment age (late Eocene) of Site 1230 (ODP Initial Report Leg 112). For the reaction transport model the rates of sulphate reduction, methanogenesis and anaerobic methane oxidation, which depend on the metabolic rates of microorganisms were found by fitting the measured ammonium porewater profiles. Figure 5 shows that at a TOC-degradation rate R_{TOC} = 0.001 mmol/l/a the modelled porewater profiles fit the measured interstitial water compositions at ODP Site 1230, measured in samples from Hole A.

Over the whole profile-depth the RT-model (RT-model 1) reproduces the reconstructed methane concentrations (from *Spivack et al., 2006*) and the measured sulphate and ammonium concentrations. The sulphate concentration continuously decreases from 28 mmol/l at the sediment-water interface to 0 mmol/l at the sulphate methane interface (SMT) at ≈ 7 mbsf. At this depth, the CH_4-concentration increases with depth. Alkalinity only reaches ≈ 100 mmol/l, which is lower than in the measured profile. DIC reaches a maximum of about 240 mmol/l at 130 mbsf, which is higher than measured DIC (but due to possible degasing after sampling, measured DIC is an inaccurate parameter).

Table 9 shows calculated alkalinity and DIC-values, which are input-parameters for the geochemical modelling. Due to the continuous increase of alkalinity and its connection with DIC through pH, each DIC-alkalinity couple equals a specific depth in ODP Site 1230 profile.

	RT Model 1			RT Model 2		
mbsf	alkalinity mmol/l	DIC mmol/l	DIC/alkalinity	alkalinity mmol/l	DIC mmol/l	DIC/alkalinity
SW	2.10	2.00	0.95	2.10	2.00	0.95
10	48.94	49.97	1.02	63.72	77.01	1.21
20	68.71	82.60	1.20	83.08	127.62	1.54
30	76.87	107.61	1.40	96.34	171.94	1.78
40	83.41	130.03	1.56	108.27	212.37	1.96
50	89.28	150.33	1.68	119.08	249.04	2.09
60	94.54	168.55	1.78	128.77	281.96	2.19
70	99.19	184.71	1.86	137.37	311.16	2.27
80	103.25	198.82	1.93	144.86	336.67	2.32
90	106.72	210.90	1.98	151.27	358.49	2.37
100	109.60	220.95	2.02	156.60	376.65	2.41
110	111.90	228.98	2.05	160.86	391.16	2.43
120	113.62	234.99	2.07	164.05	402.03	2.45
130	114.77	239.00	2.08	166.17	409.28	2.46
140	115.34	241.00	2.09	167.23	412.90	2.47
150	115.34	241.00	2.09	167.23	412.90	2.47

Table 9: Calculated alkalinity and DIC-values from the RT-model and the corresponding depth, which serve as important input-parameters for the geochemical model. RT-model 1 fits ammonium concentration of Site 1230 while RT-model 2 fits measured alkalinity.

The ratio at which the alkalinity increases relative to the DIC is critical for the carbonate equilibrium as it controls the pH and the saturation state of carbonate minerals. However, the evolution of the DIC/alkalinity ratio is not only linked to reaction stoichiometry as it also depends on diffusive transport. The DIC/alkalinity ratio can be determined from the different scenarios simulated with the reaction transport model.

Figure 6 shows the same RT-model with R_{TOC} = 0.0018 mmol/a (RT-model 2). Calculated alkalinity fits to the measured data, but the methane and ammonium concentrations differ considerably from the data. [CH_4] reaches a maximum of 250 mmol/l at a depth of about 130 mbsf, which rather coincides with values, calculated from hole B data (*Spivack et al., 2006*). The modelled ammonium concentrations are much higher than measured ones at Site 1230. However, if ammonium concentrations corrected for ion exchange with Mg are considered, the modelled profile matches well with the corrected data below ca. 100 mbsf. In the upper part of the profile, the model underestimates the corrected ammonium data.

RT-model 1:

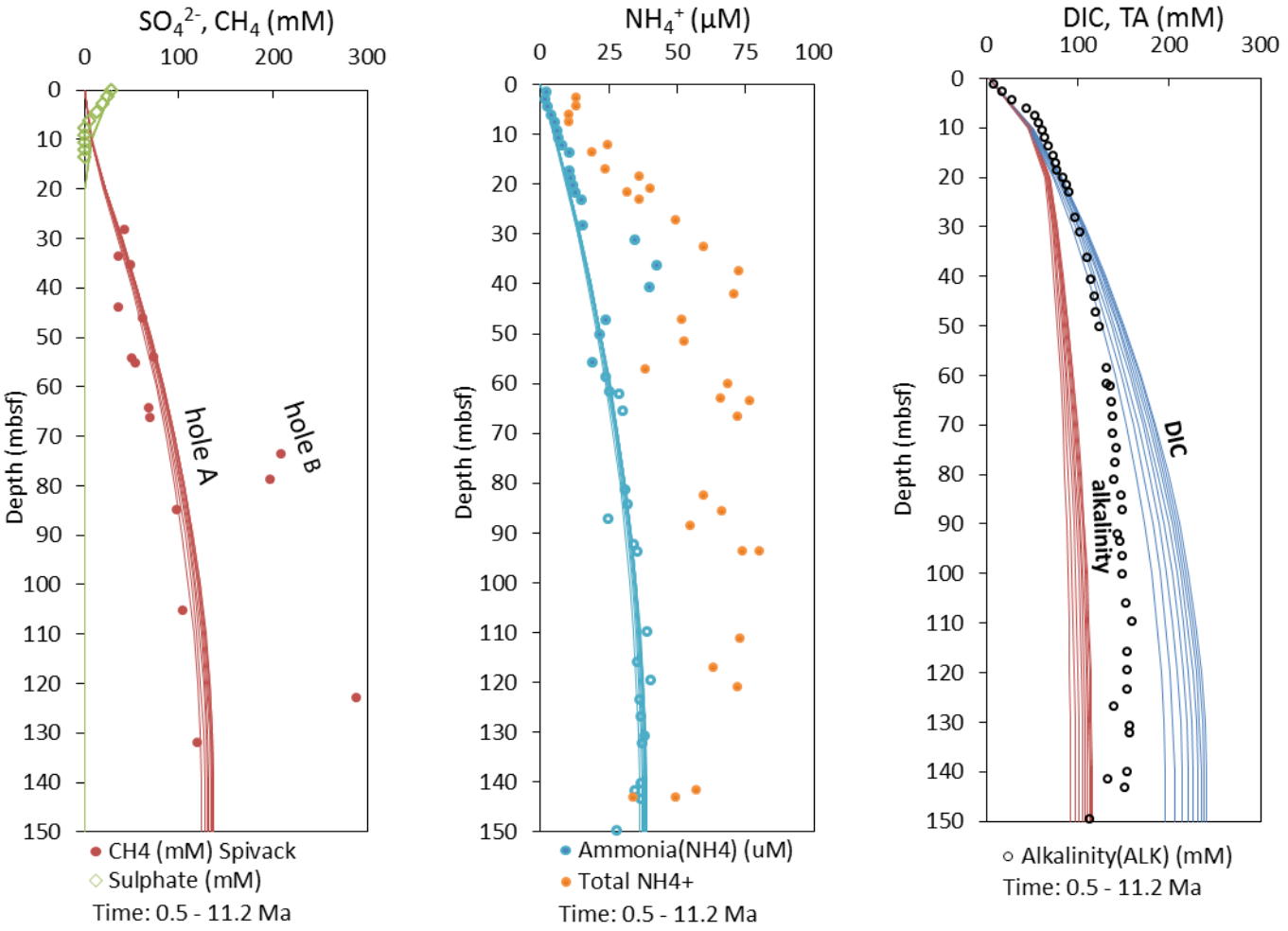

Figure 5: Measured (shown as points) and calculated (shown as lines) sulphate, methane, ammonium, DIC and alkalinity concentration of IODP Site 1230. A TOC-degradation rate of 0.001 mmol/l/a comes closest the measured concentrations of SO_4^{2-}, CH_4 and $NH4^+$. RT-model 1 fits measured ammonium concentration. TA stands for alkalinity in final solution.

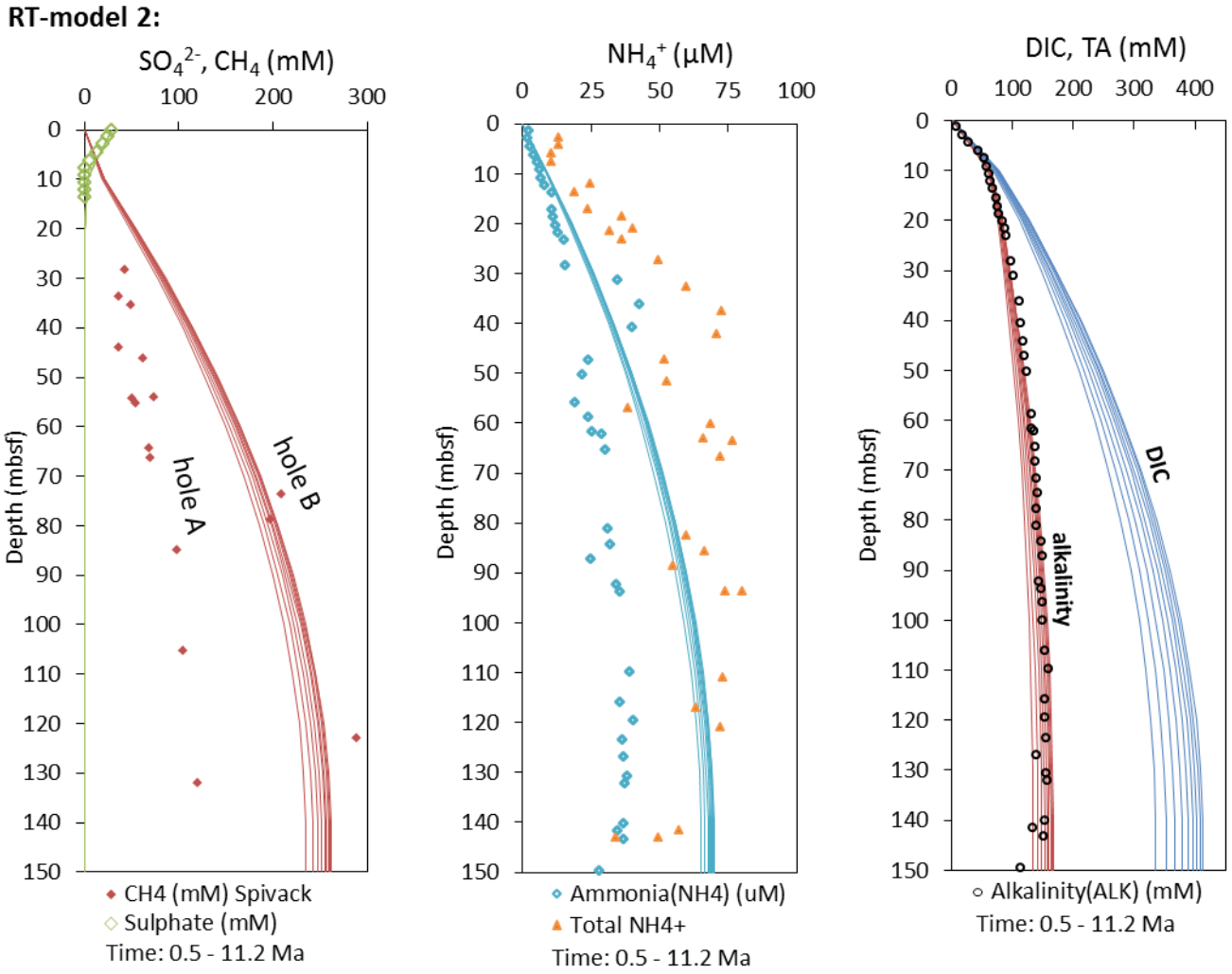

Figure 6: RT-model 2 fits the measured alkalinity of ODP Site 1230 with an TOC-degradation rate of 0.0018 mmol/l/a, but the calculated concentrations of CH_4 and NH_4^+do not follow the gradient at ODP Site 1230 (Hole A). TA stands for alkalinity in final solution

4.3 Water-mineral equilibrium model

4.3.1 Speciation and carbonate equilibrium in marine porewater

Figure 7 shows the effect of an increase in DIC on the pH at constant alkalinity (solid lines) assuming three different initial solutions with an alkalinity of 2, 200 and 450 mmol/l at 500 bar and 10°C. Furthermore, a more realistic scenario for the conditions in a methanogenic zone, assuming both alkalinity and DIC increase in the proportions calculated in RT-model 1 and 2, is plotted as points.

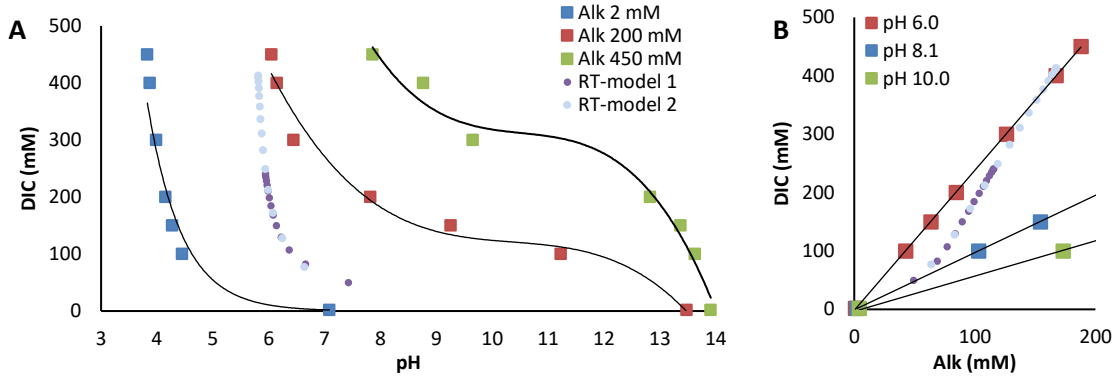

Figure 7: A: Change of pH and DIC with constant alkalinity compared with the results from reaction transport model. The shape of the curve indicates a titration-curve. B: Alkalinity and DIC development with constant pH and from reaction transport model. Increasing pH lowers the slope of the curve.

At constant alkalinity, the increase in DIC results in a lower pH of the fluid. If pH is constant (e.g because of buffer-reactions) alkalinity increases linearly with DIC, whereby the initial pH affects the slope of the curve in figure 7B.

The stepwise increase of DIC with constant alkalinity leads to a non-linear relationship between pH and DIC. So the geochemical modelling simulates a titration and the resulting points in figure 7A can be connected with a titration curve. The equivalence points, respectively the theoretical end-points of the two geochemical models are ≈ 250 mmol/l DIC for input-values from RT-model 1 and ≈ 410 mmol/l DIC for input-values from RT-model 2. Both models equilibrate at a pH of ≈ 6.

4.3.2 Saturation states of silicate and carbonate minerals in the porewater

Saturation indices were calculated for K-feldspar (K-Fsp), the clay minerals illite (Ill), kaolinite (Kao), montmorillonite (Mont), chlorite (Chl) and calcite carbonate (Cal). Additionally amorphous opal (SiO_2(a)) was considered as equilibrium phase in all saturation

calculations. Figure 8 shows the saturation states at increased DIC concentrations and constant alkalinity if no mineral reactions take place. In general, a higher concentration of DIC in seawater without alkalinity increase leads to acidification and an increase of solubility of silicates and clay minerals. Except kaolinite, all simulated minerals are undersaturated as soon as the pH of the solution reaches 5.5-5.1. At low DIC conditions the SI of chlorite, calcite and dolomite decrease most steeply with DIC increase, reaching almost minimum SI (maximum undersaturation) at about 10 mmol/l DIC. Further input hardly influences the saturation of calcite and dolomite. In contrast, the SI-curves of all other clay minerals continue to decrease with increasing DIC concentration. The SI of K-Fsp, montmorillonite and illite continuously decrease with increasing DIC and do not reach a plateau below 100 mmol/l DIC. Kaolinite needs the highest input of DIC (and the lowest pH) to reach undersaturation.

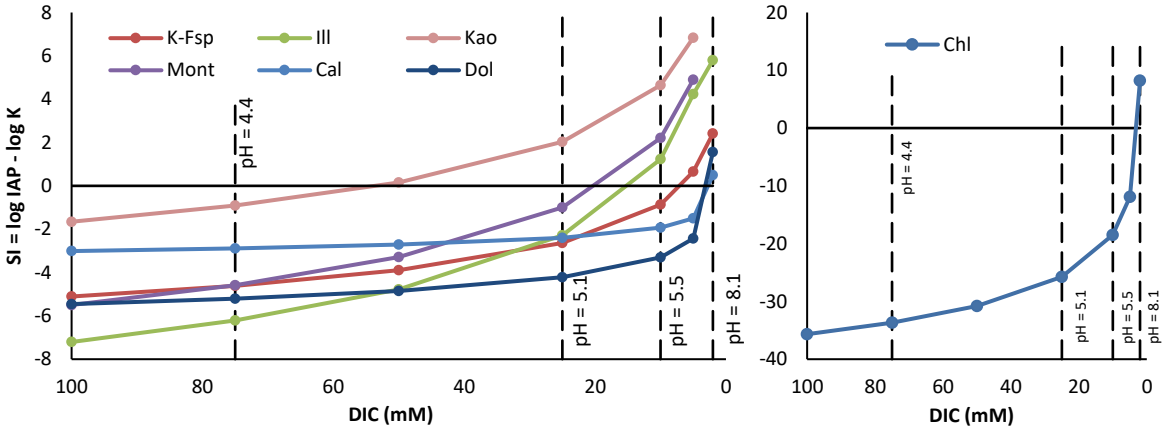

Figure 8: SI-development in a scenario of increasing DIC in seawater. Considered silicates, clay mineral and carbonates are defined by: K-Fsp = $KAlSi_3O_8$; Ill = $K_{0.6}Mg_{0.25}Al_{2.3}Si_{3.5}O_{10}(OH)_2$; Dol = $CaMg(CO_3)_2$; Cal = $CaCO_3$; Kao = $Al_2Si_2O_5$; Mont = $Mg_{0.165}Al_{2.33}Si_{3.67}O_{10}(OH)_2$; Chl = $Mg_5Al_2Si_3O_{10}(OH)_8$. The relationship of pH to DIC is simulated while alkalinity is fixed at 2.1 mM.

Equilibration reactions of 48 thermodynamically possible combinations of the minerals K-feldspar, illite, kaolinite, montmorillonite, chlorite and calcite + $SiO_2(a)$ with the aqueous solution were calculated. Table 10 shows the different mineral assemblages with their scenario number.

Szenario	Mineral Phases			Szenario	Mineral Phases			
1	Adular			25	Adular	Illite	Calcite	
2	Illite			26	Adular	Kaolinite	Montmor	
3	Kaolinite			27	Adular	Kaolinite	Chlorite	
4	Montmor			28	Adular	Kaolinite	Calcite	
5	Chlorite			29	Adular	Montmor	Chlorite	
6	Calcite			30	Adular	Montmor	Calcite	
7	Adular	Illite		31	Adular	Chlorite	Calcite	
8	Adular	Kaolinite		32	Illite	Kaolinite	Montmor	
9	Adular	Montmor		33	Illite	Kaolinite	Chlorite	
10	Adular	Chlorite		34	Illite	Kaolinite	Calcite	
11	Adular	Calcite		35	Illite	Montmor	Chlorite	
12	Illite	Kaolinite		36	Illite	Montmor	Calcite	
13	Illite	Montmor		37	Illite	Chlorite	Calcite	
14	Illite	Chlorite		38	Kaolinite	Montmor	Calcite	
15	Illite	Calcite		39	Montmor	Chlorite	Calcite	
16	Kaolinite	Montmor		40	Adular	Illite	Kaolinite	Calcite
17	Kaolinite	Chlorite		41	Adular	Illite	Montmor	Calcite
18	Kaolinite	Calcite		42	Adular	Illite	Chlorite	Calcite
19	Montmor	Chlorite		43	Adular	Kaolinite	Montmor	Calcite
20	Montmor	Calcite		44	Adular	Kaolinite	Chlorite	Calcite
21	Chlorite	Calcite		45	Adular	Montmor	Chlorite	Calcite
22	Adular	Illite	Kaolinite	46	Illite	Kaolinite	Montmor	Calcite
23	Adular	Illite	Montmor	47	Illite	Kaolinite	Chlorite	Calcite
24	Adular	Illite	Chlorite	48	Illite	Montmor	Chlorite	Calcite

Table 10: List of mineral equilibria. In addition, SiO_2 was used as equilibrium phase in every scenario.

For an equilibration, super-saturated minerals precipitate and undersaturated minerals dissolve until SI = 0 is reached. In figure 9 and 10 the quantities of single mineral phases dissolved or precipitated (scenarios 1 to 6) in combination with SiO_2(a). Equilibrations are shown for seawater with stepwise increasing DIC. Negative values indicate precipitation and positive values indicate dissolution. Generally the quantity of the reacting minerals rises with increasing DIC. Due to the strong pH/DIC dependence, calcite (scenario 6) is most affected by DIC change as it shows the highest amount of dissolved mineral.

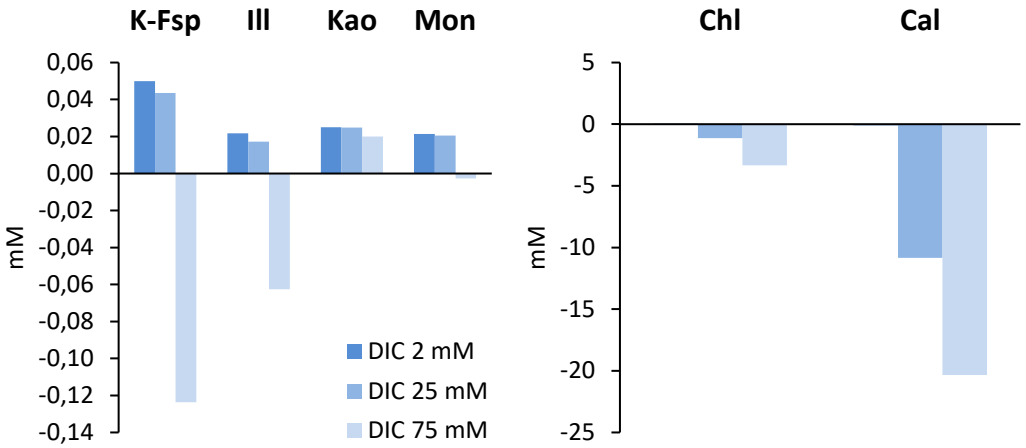

Figure 9: Quantities of mineral reactions to reach equilibrium with a stepwise increase of DIC (and constant alkalinity). Positive values mean the amount of precipitation and negative ones stand for dissolution. For equilibrium, the amount of chlorite and calcite is much higher than feldspar, illite, kaolinite and montmorillonite.

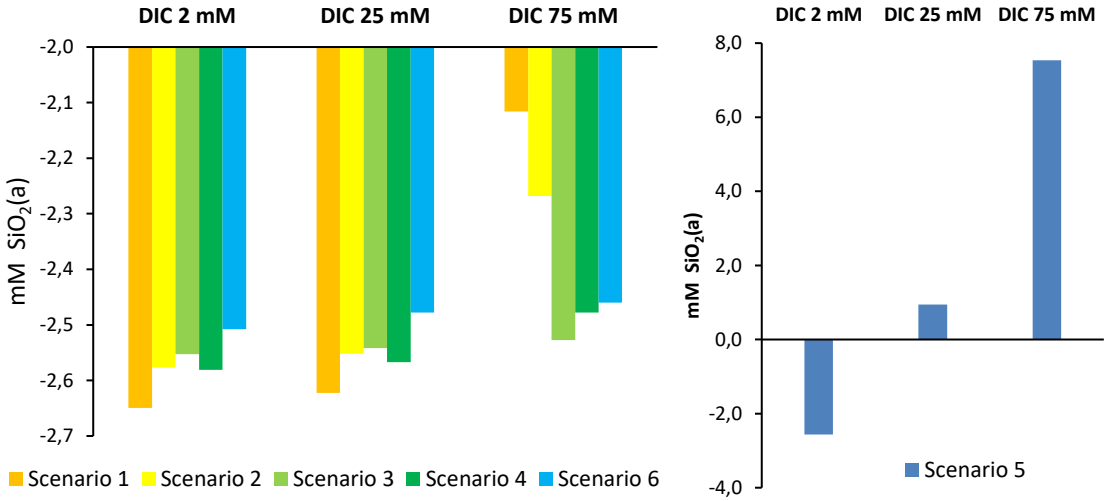

Figure 10: Quantities of amorphous Opal to reach equilibrium with a stepwise increase of DIC (and constant alkalinity). Positive values mean the amount of precipitation and negative ones stand for dissolution.

Compared with single mineral reactions, multi-mineral equilibria calculations show very different patterns especially for the quantity of involved phases. Scenarios 43-48 shown in figure 11 are combinations with the highest number of coexisting phases (4 + SiO_2(a)) that is thermodynamically possible. The quantities of dissolved or precipitated minerals reach up to 60-80 mmol/l in seawater, which therefore has the potential for strong cation-enrichment or -depletion in the final solution. For each mineral assemblage the amount of minerals reacting is the result of the speciation of the solution.

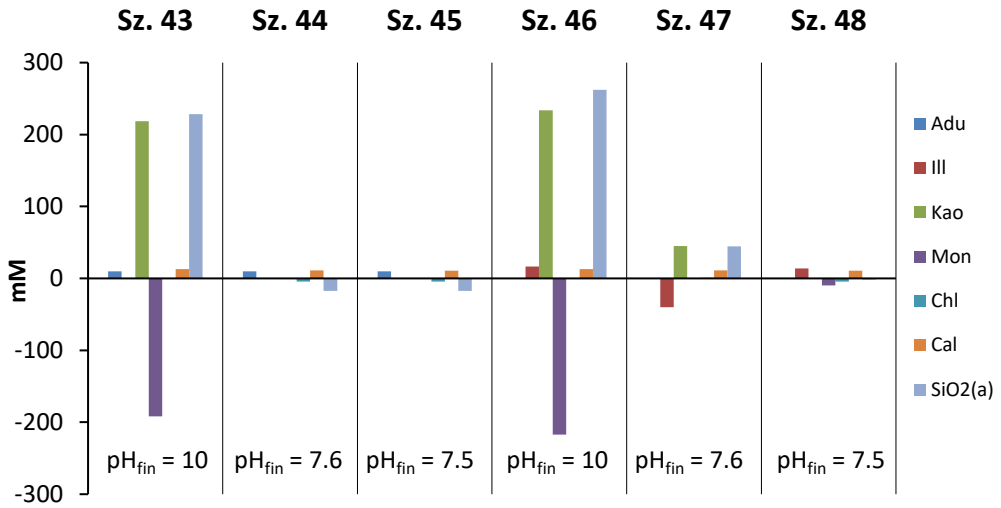

Figure 11: Amount of dissolved or precipitated minerals in scenario 43-48. Especially the combination of kaolinite and montmorillonite leads to very high amounts of reacting minerals. In addition pH of the final solution (pH_{fin}) are shown.

4.3.3 Effect of mineral equilibration on ionic concentrations in the porefluid

Dissolution and/or precipitation of minerals change the chemistry of a solution. Figure 12 shows the ion concentrations in the fluid after the stepwise increase of DIC in seawater and subsequent equilibrium reactions with all possible combinations of feldspar, illite, kaolinite, montmorillonite, chlorite and calcite + SiO_2(a). If no mineral reacts the initial cation concentration of the seawater equals the final one. The K^+-concentration is affected by reactions with K-feldspar and illite, the Mg^{2+}-concentration by illite, montmorillonite and chlorite, and the Ca^{2+}-concentration only by calcite. All scenarios show relatively low quantities of reacting minerals but a large effect on solute composition of the fluid. Especially equilibrium reactions of e.g scenarios 13, 33 and 35 have the potential for strong changes of the solution.

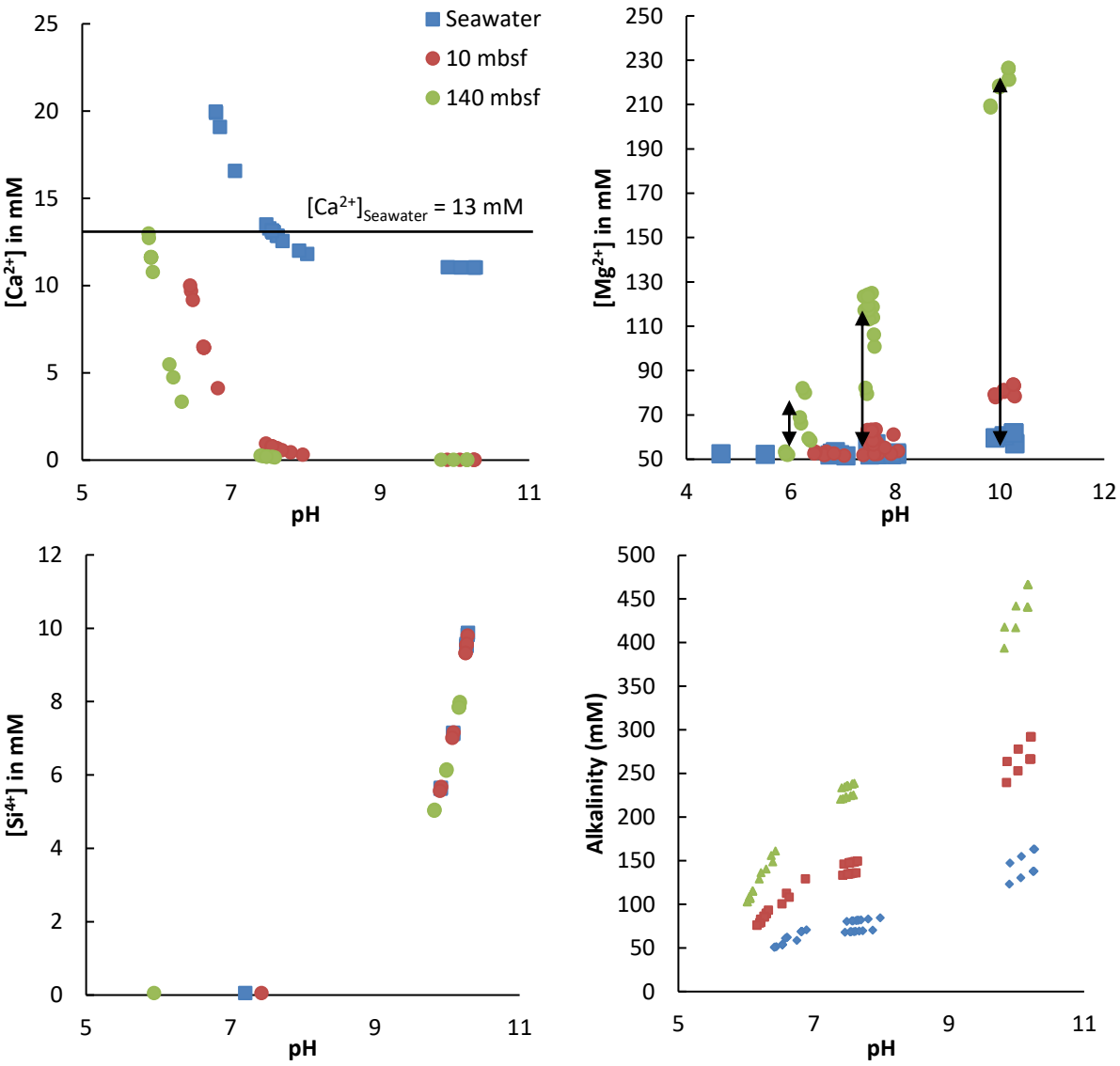

Figure 12: Cation composition and alkalinity of final solution after stepwise increase of DIC. All possible combinations of feldspar, illite, kaolinite, montmorillonite, chlorite and calcite + SiO_2(a) were calculated. The black line shows the initial concentration of standard seawater.

There are several pathways of how mineral equilibria change the cation concentration of the solution. There are reactions, which consume at least one cation nearly completely because of precipitation of one or more minerals containing the element. The final composition of such solutions may show a limitation of distinct cations. With input-parameters from RT-model 1 and 2, there is no mineral combination, which produces a solution with more than the initial 13 mmol/l Ca^{2+}, although many scenarios release high quantities of Mg^{2+} and K^{+}. Especially four scenarios (no. 26, 32, 43 and 46) strongly enrich the final solution in Mg^{2+} (figure 12).

A decreased pH normally leads to increased dissolution of calcite, which should increase Ca^{2+} concentration of the final solution. Only some scenarios with seawater chemistry (no. 34, 37-38, 40-41, 43-44 and 46-47) lead to a final [Ca^{2+}] of greater than 13 mmol/l.

The increasing alkalinity (input-parameters from RT-model 1) between 10 and 140 mbsf oversaturates calcite in all scenarios. Therefore, calcite precipitation is part of all equilibrium reactions of scenarios, which consider calcite. Alkalinity of the final solution largely depends on the quantity of precipitated calcite.

The equilibrium with SiO_2(a) partially compensates for the Si^{4+} released during silicate dissolution. The solubility of any other minerals is then limited by other ions, e.g. Al^{3+}. Especially the combination kaolinite and montmorillonite (scenarios 16, 26, 32, 38, 43 and 46) leads to strong Si^{4+} enrichment, but Si^{4+} is removed (buffered) by SiO_2(a). Figure 12 also shows that an increase of DIC does not change the direction of a reaction, i.e. precipitation or dissolution of a mineral.

4.3.4 Effects of mineral reactions on pH and DIC

Depending on the involved minerals, precipitation or dissolution will have different effects on pH, DIC and alkalinity. Figure 12 shows that all mineral equilibria lead to low (6-7), intermediate (7-9) or high (≈ 10) final pH-values. At constant DIC, the alkalinity corresponds with final pH through a titration curve with two end points at low and high pH (Fig. 11). The pH increase results from the quantity of reacting minerals mostly limited by [Al^{3+}] of the solution. All scenarios with high final alkalinity and pH show high quantities of reacted minerals. The net-alkalinity change of the solution results from the difference of alkalinity production by the dissolving minerals and alkalinity consumption by the precipitating minerals. Increasing DIC does not affect alkalinity, unless the system is strongly buffered. So, due to cation enrichment, more soluble minerals lead to a high alkalinity.

4.3.5 Fitting measured porewater-profiles

The final composition of seawater, after equilibration with all possible combinations of feldspar, illite, kaolinite, montmorillonite, chlorite and calcite + SiO_2(a) was compared with measured porewater from ODP Site 1230 to find the best matching scenario. The equilibrium-reaction of calcite and chlorite + SiO_2(a) (scenario 21) with input-parameters from RT-model 1 fits best to the measured alkalinity and porewater cation concentrations from ODP Leg 201, Site 1230 (*D'Hondt et al., 2003*; *Donohue et al., 2006*). Figure 13 shows the final composition of the solution after equilibrium of the best fitting scenario 21 (chlorite, calcite + SiO_2(a)) and for comparison scenario 5 (chlorite + SiO_2(a)) and 6 (calcite + SiO_2(a)) with the input-parameters of (1) RT-model 1 and (2) RT-model 2. Between 60 and 140 mbsf the modelled alkalinity matches very well with the measured profile. Scenarios 5, 6 and 21 are characterised by the absence of other clay minerals and K-feldspar, hence, $[K^+]$ and $[Mg^{2+}]$ are not significantly affected. The potassium concentration increases from ≈ 12 mmol/l at 10 mbsf to ≈ 14 mmol/l in 60 mbsf, which indicates a K^+-source in the shallower sediment. The deeper sediment column between 60 and 160 mbsf shows no significant change in $[K^+]$.

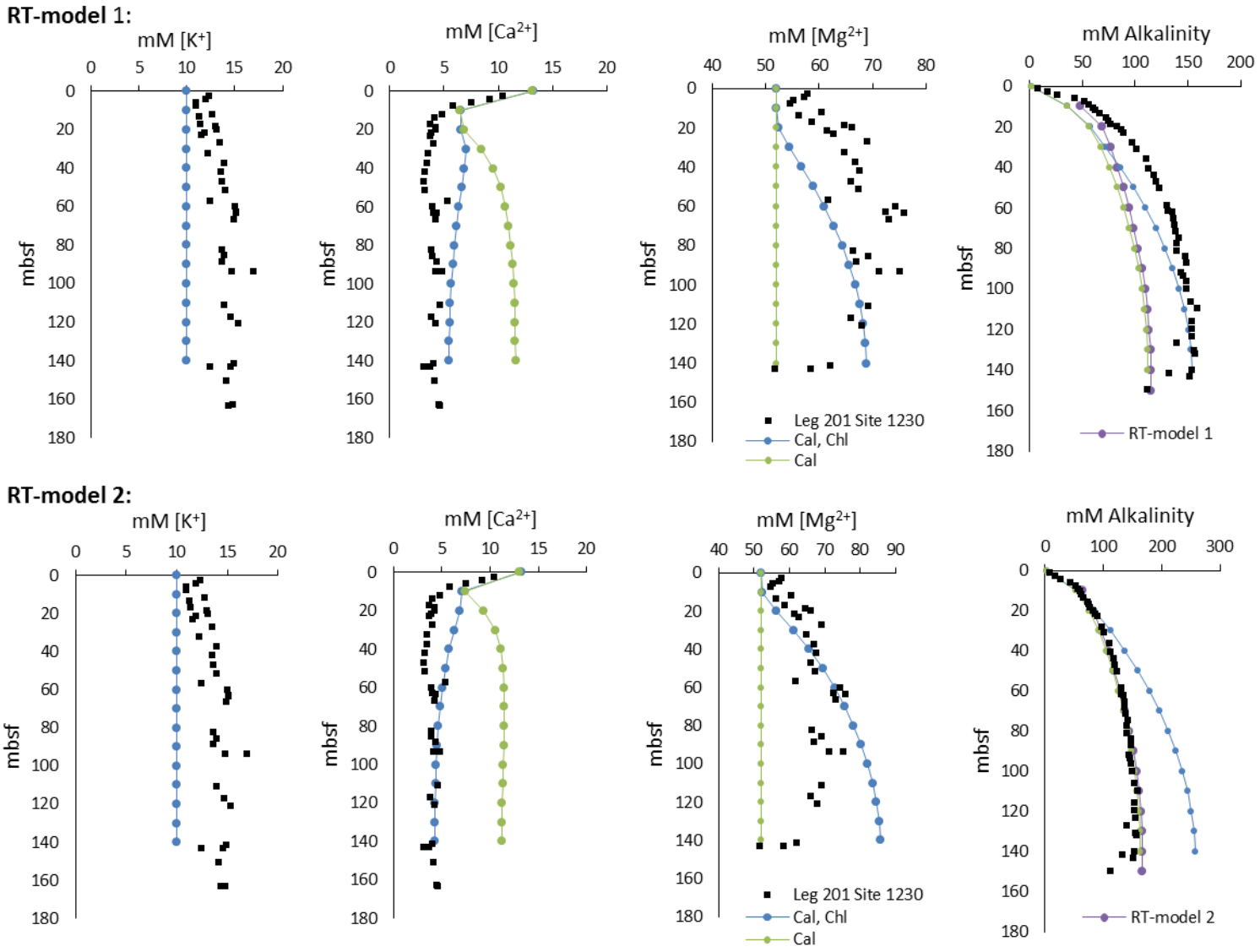

Figure 13: Measured and calculated concentrations of the major cations K^+, Ca^{2+}, Mg^{2+} and alkalinity from ODP Site 1230. The solid lines named RT-model 1 and 2 show the alkalinity of the initial solution.

No scenario (initial alkalinity and DIC taken from RT-model) reproduces the measured concentration of magnesium in interstitial water precisely. Either the amount of dissolving Mg-bearing minerals is too low to increase [Mg^{2+}] in the final solution significantly (scenarios 6, 7, 11, 15, 18 and 20) or the equilibrium reaction releases enormous quantities of magnesium with depth (e.g scenarios 23 and 46), which do not fit measured Mg^{2+}-profile.

Scenarios which fit measured chemistry of ODP Site 1230 best, have a similar or higher amount of aluminum in final solution, whereas all other scenarios almost entirely deplete [Al^{3+}] from initial seawater (0.05 mmol/l). Table 11 shows the amount of dissolved and precipitated minerals for equilibration in the case of scenario 5, 6 and 21 (chlorite + SiO_2(a); calcite + SiO_2(a); chlorite, calcite + SiO_2(a)) with input-parameters from RT-model 1 and 2.

RT model 1 **RT model 2**

Chlorite Equilibrium (scenario 5)

mbsf	pH	Chl (mmol/l)	Cal (mmol/l)	SiO_2 (mmol/l)	Alkalinity (mmol/l)	DIC (mmol/l)	pH	Chl (mmol/l)	Cal (mmol/l)	SiO_2 (mmol/l)	Alkalinity (mmol/l)	DIC (mmol/l)
0	8.10	0.02	--	-2.57	2.27	2.00	8.10	0.02	--	-2.57	2.27	2.00
10	7.38	0.03	--	-2.56	48.54	49.97	6.63	0.01	--	-2.52	63.51	77.01
20	6.65	0.01	--	-2.53	68.48	82.60	6.32	-0.48	--	-1.02	90.84	127.62
50	6.28	-0.95	--	-2.48	104.53	150.33	6.19	-2.93	--	6.34	165.97	249.04
130	6.19	-2.80	--	5.96	159.64	239.00	6.13	-6.13	--	16.00	265.46	412.90

Calcite Equilibrium (scenario 6)

mbsf	pH	Chl (mmol/l)	Cal (mmol/l)	SiO_2 (mmol/l)	Alkalinity (mmol/l)	DIC (mmol/l)	pH	Chl (mmol/l)	Cal (mmol/l)	SiO_2 (mmol/l)	Alkalinity (mmol/l)	DIC (mmol/l)
0	8.10	--	7.10	-2.51	2.27	2.00	8.10	--	7.10	-2.51	2.27	2.00
10	6.63	--	6.56	-2.50	35.82	43.41	6.41	--	5.58	-2.49	52.55	71.43
20	6.42	--	6.15	-2.49	56.40	76.45	6.17	--	3.68	-2.48	75.72	123.94
50	6.09	--	2.80	-2.48	83.69	147.53	5.92	--	1.62	-2.46	115.84	247.42
130	5.92	--	1.40	-2.46	112.55	239.60	5.80	--	1.75	-2.44	163.74	411.15

Chlorite+Calcite Equilibrium (Scenario 21)

mbsf	pH	Chl (mmol/l)	Cal (mmol/l)	SiO_2 (mmol/l)	Alkalinity (mmol/l)	DIC (mmol/l)	pH	Chl (mmol/l)	Cal (mmol/l)	SiO_2 (mmol/l)	Alkalinity (mmol/l)	DIC (mmol/l)
0	8.10	0.03	-1.18	-2.58	2.27	2.00	8.10	0.03	-1.18	-2.58	2.27	2.00
10	6.63	0.01	7.40	-2.57	35.72	43.47	6.43	-0.09	5.92	-2.22	53.35	71.09
20	6.44	-0.09	7.52	-2.53	57.22	76.16	6.28	-0,87	6.12	1.19	84.69	121.50
50	6.24	-0.46	6.30	-0.95	98.77	143.95	6.17	-3.48	7.65	7.98	159.43	241.39
130	6.17	-3.34	7.23	2.90	154.48	233.47	6.12	-6.73	8.76	17.79	257.53	404.14

Table 11: Amount of precipitated or dissolved minerals with depth, to reach equilibrium in the case of the best fitting scenarios 5, 6 and 21. Input-parameters are from RT-model 1 and 2.

5. Discussion

5.1 Sediment composition and possible mineral reactions

Bulk XRD shows a mineral composition of fine grained sediments with detrital continental input of quartz, feldspar and mica as dominant silicate phases. The X-ray pattern of the < 2 µ grain-size fraction of all samples (figure 4) shows elevated baselines, which indicates a large share of amorphous opal from diatom frustules. This is typical for biogenic deep-sea sediments consisting of diatom-ooze with various amounts of siliciclastic components described in ODP Site 1230 (*ODP Initial Report Leg 112*). Therefore, assumed equilibrium with opal A (SiO_2(a)) in every calculated scenario seems to be realistic.

Analysed samples contain various amounts of illite, kaolinite, chlorite and smectite-group minerals. Except a tendency for smaller chlorite-peaks in the deeper sediment and the occurrence of calcite in samples from 60 to 140 mbsf, there is no significant change in the peak patter with depth, which may indicate very low rates of silicate alteration. However, geochemical modelling of mineral equilibria showed that the precipitation or dissolution of only small amounts of (clay) minerals may lead to strong changes in the chemistry of the solution (figure 12).

XRD-Analysis itself provides no clear information about the time of mineral precipitation. Due to CO_2 degassing and temperature increase after sampling, ex-situ carbonate precipitation may play a role. Equation 16 shows the calculation to estimate the quantity of carbonate precipitation after sampling.

$$\frac{[Ca^{2+}]_{SW} \cdot M_{CaCO_3}}{(1-\varphi) \cdot \rho} = [CaCO_3]_{Pr} \quad \textbf{Eq. (16)}$$

But a porewater concentration of 4 mmol/l Ca^{2+} (table 12; figure 13) only allows a total precipitation of about 1 g $CaCO_3$ per 1000 g sediment, which is far below the detection limit of the XRD-method.

Parameter	Description	Value
$[Ca^{2+}]_{SW}$	$[Ca^{2+}]$ of porewater	4 mM
M_{CaCO3}	Molar mass $CaCO_3$	100.0864
φ	Sediment porosity	0.7
ρ	Sediment density	1.4 kg/l
$[CaCO_3]_{Pr}$	Maximum amount of precipitated Calcite	0.1 wt%

Table 12: Parameters for the calculation of maximum amount of $CaCO_3$ precipitation

Porewater Ca-concentration sharply decreases near the surface and stays constant at ≈ 4 mmol/l below 15 mbsf, which may be explained by diagenetic carbonate precipitation. An increased Mg-content in calcite leads to a decreased d-space of the crystal lattice and a larger 2 Theta-angle. The Mg content of calcite can be determined by a shift of the 104 peak using the equation of *Lumsden (1979)*. While XRD from the shallow sediment (6.3 mbsf) shows only one Mg-free calcite peak, a double peak indicates two types of calcite in deeper samples (60 - 140 mbsf): A "pure calcite" (similar to the calcite peak from 6.3 mbsf) and a Mg-bearing calcite, which follows a downcore decrease in $[Mg^{2+}]$ concentration of the porewater below 70 mbsf (figure 13).

A dolomite bed at 6.5 mbsf (*see Meister et al., 2007*) is precipitated under the influence of sulphate reduction or AOM and the interval between 50 and 60 mbsf within the zone of methanogenesis seems to be calcite-free. The porewater in this interval is characterised by a strong downward increase in alkalinity (figure 13).

5.2 Biogeochemical reactions and effects on porewater chemistry

In the deeper sediment, microbial produced alkalinity (calculated in the RT-model 1 and 2) does not entirely explain measured alkalinity (although this depends on the scenario). Simultaneously, the downcore change of the concentration gradient of the major cations K^+ and Mg^{2+} indicates cation release in the sediment column of ODP Site 1230 (figure 13).

For quantifying the content of microbial produced alkalinity, measured ammonium concentration was recalculated with a reaction transport model (diffusion model). In general, the ammonium concentration, caused by fermentation, is a reliable parameter for the quantification of microbial activity rates (*Heini et al., 2015*).

A TOC degradation-rate (s_{TOC}) = 0.001 mmol/l/a from reaction transport model 1 (figure 5) fits calculated ammonium concentrations best and leads to an alkalinity of up to 115 mmol/l in 140 mbsf. Only measured $[NH_4^+]$ between 30 and 40 mbsf is twice as high as the calculated one and may be caused by a downward decreasing organic-matter degradation rate within the top 40 metres of sediment or differences in cation-exchange rates between upper and lower profile. $[CH_4]$ from RT-model 1 perfectly fits the concentration of methane calculated by *Spivack et al. (2006)*.

The comparison between RT-model 1 and 2 shows that even small variations in s_{TOC} leads to great changes in geochemical profiles. Alkalinity calculated by increasing the s_{TOC} to 0.0017 mmol/l/a (RT-model 2; figure 6) fits perfectly measured alkalinity, but this scenario does not reproduce measured ammonium concentration of Site 1230. In addition, resulting methane concentrations of RT-model 2 are far too high to fit the data from hole A but they rather fit the

values from Hole B.

Compared with a measured alkalinity of up to 150 mmol/l, RT-model 2 does not need an additional source of alkalinity. Both RT-models show that sulphate reduction, AOM and ammonium release lead to high alkalinity but only RT-model 1 fits measured ammonium concentration.

Sulphate reduction and AOM between 0 and 30 mbsf lead to an increase of +1 alkalinity per CH_2O (for SR) and +2 alkalinity per CH_2O (for AOM) in porewater through HS^- and HCO_3^- release. So the first 30 mbsf are characterised by a strong increase in porewater alkalinity. Additionally, NH_4^+ remineralisation during degradation of OM takes place within the whole sediment column. Below the SMTZ (≈ 10 mbsf) methanogenesis causes no change in alkalinity and an increase in DIC of the porewater, but microbial ammonium release produce +1 alkalinity per consumed NH_3.

This indicates a compensation of acidification by an increase in DIC through microbial alkalinity production rather than a strong pH-buffer effect as a result of clay mineral equilibrium or by upward migrating deeper fluids assumed by *Wallmann et al. (2008)* and *Meister et al. (2011)*.

Dissolution of undersaturated mineral phases may produce additional porewater alkalinity and may close the gap between microbial produced alkalinity and measured alkalinity in porewater.

5.3 Effects of biogeochemical reactions on mineral saturation states

Different input-parameters for initial solution from RT-model 1 and 2 lead to different saturation states of the mineral phases K-feldspar, illite, kaolinite, montmorillonite, chlorite, calcite and SiO_2(a), which are shown in figure 14.

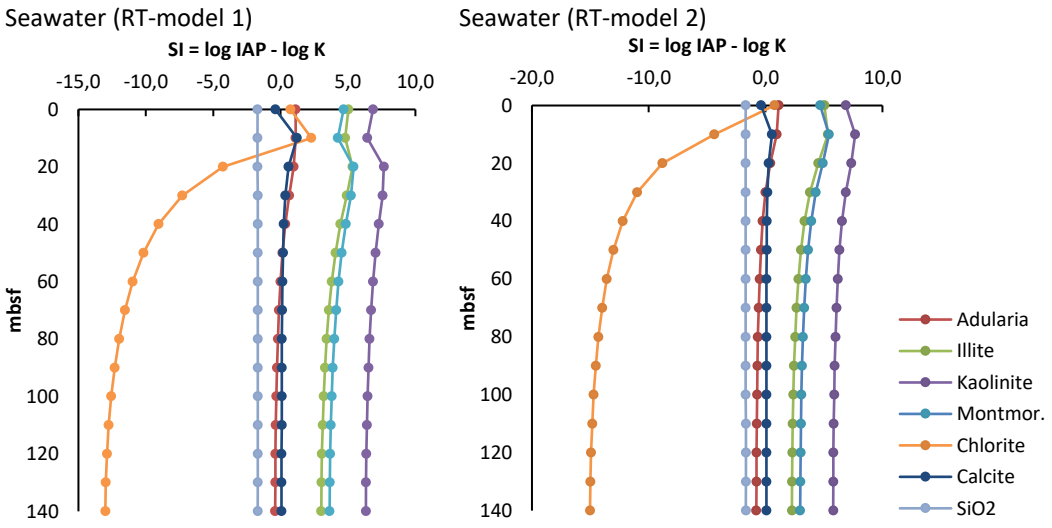

Figure 14: Initial SI of the silicate and carbonate phases in seawater changes with increasing alkalinity and DIC respectively depth. Both RT-models show positive carbonate saturation, which is the requirement for precipitation. The input-parameters alkalinity and DIC for SI calculation were taken from RT-model 1 and 2 (table 5 and 8).

Increasing acidification (figure 7, 14 and 15) leads to a decrease of the saturation indices of all silicate phases and calcite. The transition of chlorite oversaturation to undersaturation in seawater with input-parameter from RT-model 1 moves towards a more shallow depth in the porewater with input-parameters from RT-model 2. Generally the release of high amounts of alkalinity leads to a rapid change of mineral saturation in the first 20 mbsf.

The influence of iron reduction and cryptic sulphur cycling on the alkalinity of the porewater was not considered. Only within sediments of the sulphate-reduction zone (about 0-10 mbsf), sulphide formation generates additional alkalinity. Equation 17 shows the formation of pyrite:

$$8\ FeO(OH) + SO_4^{2-} + 15\ HS^- + 17\ H^+ \rightarrow 8\ FeS_2 + 20\ H_20 \quad \textbf{Eq. (17)}$$

The reaction needs a small amount of sulphate because the iron cannot oxidise enough sulphide to produce FeS_2. For each mole of pyrite approximately 0.25 mol alkalinity are produced. Assuming that all sulphide immediately precipitates as pyrite, additional 0.125 mole of alkalinity is produced per mole of sulphate turned over. Some of the sulphide escapes upwards by diffusion, so the real contribution to alkalinity is probably smaller. Thus, the overall effect of reductive dissolution of Fe (III) and pyrite formation is rather small.

Due to missing data of $[Al^{3+}]$ from Site 1230 also the influence of Al-hydroxide formation/dissolution on alkalinity was not considered. Al-oxides are very insoluble, and the quantities of dissolved Al^{3+} do not significantly affect alkalinity.

RT-model 1 and 2 show, that the rate of TOC degradation (s_{TOC}) affects the DIC/alkalinity of the final solution (respectively porewater). Ammonium release increases the alkalinity but has no net effect on porewater DIC. High rates of methanogenesis due to a high content of preserved TOC leads to a faster increase in DIC with respect to alkalinity, which causes acidification. Figure 15 shows the change in DIC/alkalinity as well as the SI of calcite, which is one of the most affected mineral phase related to a pH-change.

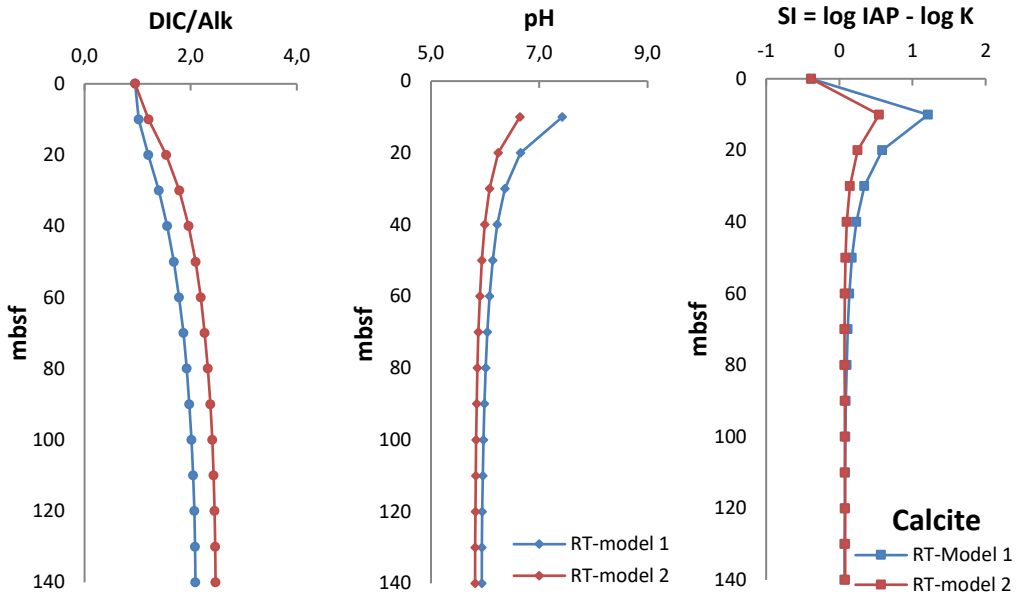

Figure 15: DIC/alkalinity ratio, pH and calcite-saturation of solution calculated with RT-model 1 (blue line) and 2 (red line).

Under conditions of increased DIC and alkalinity, calculated with model 1 and 2, the calcite-saturation stays $SI_{Cal} > 0$ through the whole depth range. pH-buffering through microbial alkalinity production prevents the final solution from lowering the pH, resulting from the input of calculated 250 mmol/l DIC. Both RT-models show that the main contribution to final alkalinity comes from microbial activity and possible mineral reactions at ODP Site 1230 play an important role.

Summarised, (clay) mineral reactions may provide a source for (1) the increase in K^+- and Mg^{2+}-porewater concentration with depth and (2) the ≈ 35 mmol/l alkalinity which are missing to reach the 150 mmol/l measured alkalinity in ODP Site 1230.

5.4 Mineral reactions and their effect on porewater chemistry

5.4.1 Clay minerals

XRD-analysis identifies various amounts of feldspar, illite, kaolinite, chlorite, smectite-group minerals and calcite in sediment samples from Site 1230. Equilibrium calculations of all possible combinations of these minerals + SiO_2(a), show the potential for increasing alkalinity in the final solution. Many scenarios lead to a strong enrichment of cations in the porewater due to dissolution of minerals. Cations are not just removed as free ions, but always in oxide form. Otherwise the mineral would become electrically charged. The oxide produces alkalinity upon water uptake and hydroxyl release. Equation 18 and 19 show the dissociation-reactions of cation-oxides and alkalinity production on the example of chlorite:

Chlorite: $Mg_5Al_2Si_3O_{16}(OH)_8$

Oxides: 5 MgO
1 Al_2O_3
3 SiO_2
4 H_2O

Reaction in solution:
$MgO + H_2O \rightarrow Mg^{2+} + \mathbf{2\ OH^-}$
$Al_2O_3 + 3H_2O \rightarrow 2\ Al^{3+} + \mathbf{6\ OH^-}$

$5\ MgO + Al_2O_3 + 4\ H_2O \rightarrow$
$5\ Mg^{2+} + 2\ Al^{3+} + \mathbf{16\ OH^-}$ **Eq. (18)**

By subtracting parts of the H_2O eq. 18 can be written in the following form:

$$Mg_5Al_2Si_3O_{10}(OH)_8 + 16\ H^+ \rightarrow 5\ Mg^{2+} + 2\ Al^{3+} + 3\ H_4SiO_4 + 6\ H_2O \quad \textbf{Eq. (19)}$$

The congruent dissolution of 1 mol chlorite theoretically consumes 16 mol of H^+, but in reality minerals are incongruently dissolved. The congruent dissolution of silicate phases would enrich the final solution strong with silica and precipitation leads to the opposite. Already a low content of 0.05 mmol/l initial SiO_2(aq) (table 6) would inhibit relevant amounts of mineral precipitation. In the geochemical model presented here, incongruent dissolution is mimicked by congruent dissolution and re-precipitation of another mineral phase. Since opal A shows a high solubilty and it is abundant in the analysed samples (based on microscopic inspection; D'Hondt et al., 2003) SiO_2(a) is used as a silicon buffer as additional phase in all calculated mineral equilibria.

5.4.2 Single mineral reactions

Precipitation or dissolution of a mineral until equilibrium with the solution leads to consumption or release of cations which may have an effect on final alkalinity. Figure 16 shows the change of seawater chemistry through SiO_2(a)-, chlorite- and calcite- equilibrium in the case of DIC and alkalinity increase calculated with RT-model 1 and 2. Equilibrium between porewater and SiO_2(a) produces a SiO_2(aq) enrichment with respect to seawater (where opal A is undersaturated). Both models show an acidification of the solution (figure 15) which causes a decrease of the solubility of SiO_2(a). The kink of the SiO_2(aq) and alkalinity profiles at 10 mbsf marks the transition from DIC/alkalinity < 1 to DIC/alkalinity > 1. SiO_2(a) dissolution is only controlled by the final pH set by alkalinity and DIC from RT-model 1 and 2. The equilibrium reactions of SiO_2(a) with seawater do not affect the final alkalinity and DIC/alkalinity.

The speciation of porewater does not lead to oversaturation of chlorite through the whole profile-depth and so there is chlorite precipitation (+ SiO_2(a) dissolution) at pH > ≈ 6.5 and the opposite

reaction at pH < ≈ 6.5. Seawater with alkalinity and DIC values from RT-model 1 has this pH-transition between 30 and 40 mbsf. A great difference between chlorite precipitation and dissolution is the reaction quantity. Only very low precipitation of ≈ 10^{-5} mmol/l chlorite does not have an influence on alkalinity, but the dissolution of up to 3.3 mmol/l chlorite strongly affects the final solution (through H^+ consumption, table 11). The equilibrium of chlorite + SiO_2(a) (scenario 5) with an initial solution influenced by TOC-degradation rate from RT-model 1 produce measured alkalinity of ODP Site 1230. Scenario 5 does not include any carbonate phase, so the reaction cannot reproduce measured [Ca^{2+}] profile.

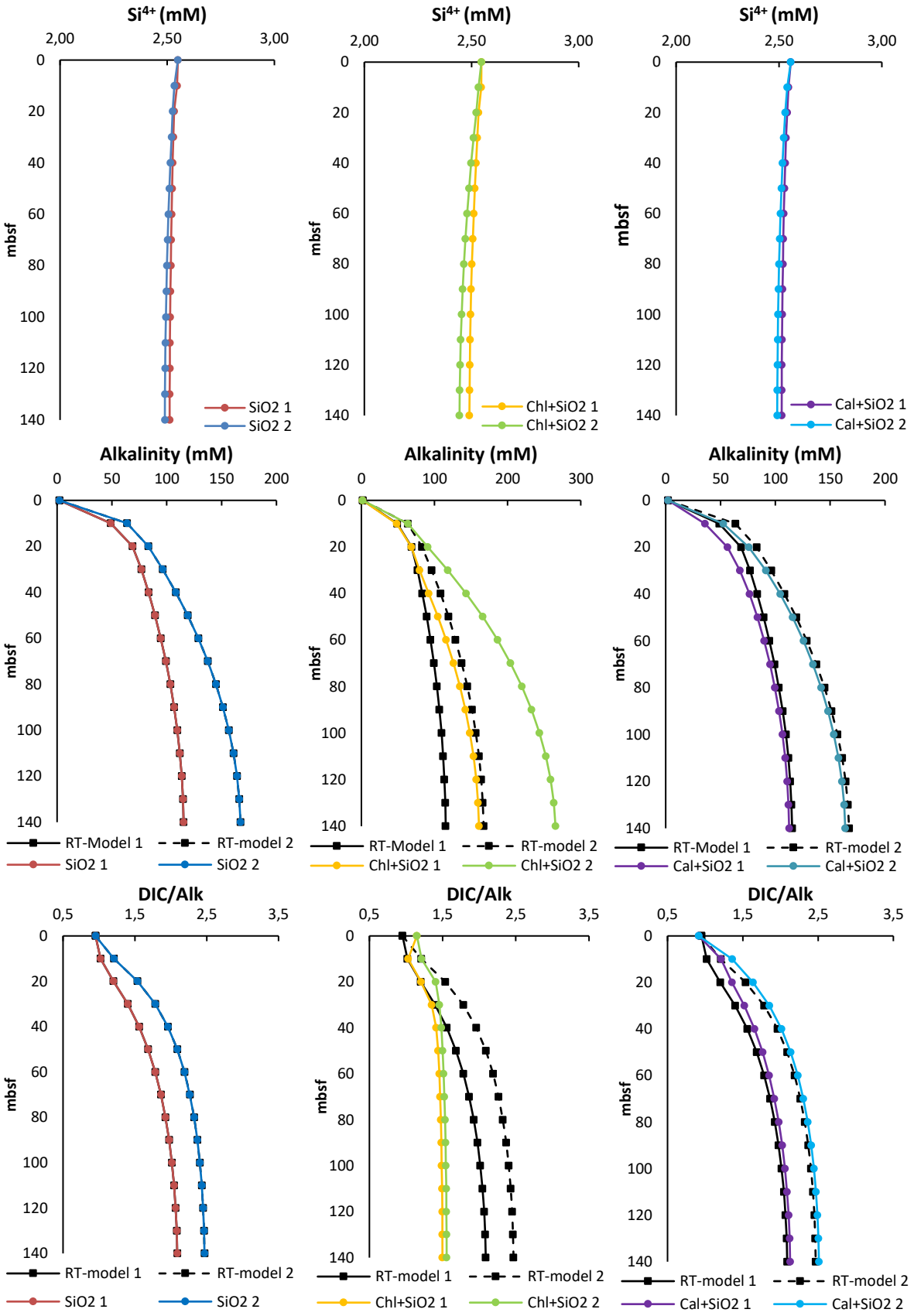

Figure 16: Calculated [Si^{4+}], alkalinity and DIC/alkalinity of final solution after equilibrium with just SiO_2(a) (SiO2 1, 2), chlorite + SiO_2(a) (Chl+SiO2 1, 2; scenario 5) and calcite + SiO_2(a) (Cal+SiO2 1, 2; scenario 6). The black lines show calculated initial alkalinity and DIC/alkalinity from RT-model 1 and 2. The numbers 1 and 2 indicates if the input-parameters for the initial solution were taken from RT-model 1 or 2.

Only equilibration with calcite can explain the measured Ca^{2+}-concentration profile. With the assumed TOC-degradation rates of RT-model 1 and 2, biogeochemical activity leads to an oversaturation of the porefluid with respect to calcite, which leads to precipitation below the top few metres of the profile. The DIC/alkalinity ratio given by the reaction stoichiometry controls the pH in the porefluid. Carbonate precipitation (scenario 6) consumes alkalinity which leads to an increased DIC/alkalinity with respect to the speciation of the initial solution. Final solution after chlorite + SiO_2(a) (scenario 5) equilibrium comes close measured porewater chemistry of Site 1230 if initial solution shows alkalinity and DIC calculated with RT-model 1 (figure 13). After equilibrium of scenario 5 with a solution characterised by input-parameters from RT-model 2, final alkalinity increases up to 266 mmol/l, which is far higher than observed. The simultaneous occurrence of chlorite and calcite between 60 and 130 mbsf indicates both reactions together (scenario 21) as possible source for measured high alkalinity.

5.4.3 Multi mineral reactions

Especially scenarios with more than 3 minerals in equilibrium (scenarios with numbers >39; table 10) have the potential to increase alkalinity by cation release. The geochemical model shows all thermodynamically possible combinations of K-feldspar, illite, montmorillonite, kaolinite and calcite + SiO_2(a) to identify the combination which comes closest to the true porewater chemistry of ODP Site 1230.

Scenario 21 (calcite, chlorite + SiO_2(a)), calculated with the PHREEQC-code may explain a high alkalinity of up to 150 mmol/l from porewater of ODP Site 1230 best. Figure 17 shows the calcite-saturation states of the final solution after equilibrium with chlorite + SiO_2(a) (scenario 5) and chlorite-saturation states of the final solution after equilibrium with calcite + SiO_2(a) (scenario 6).

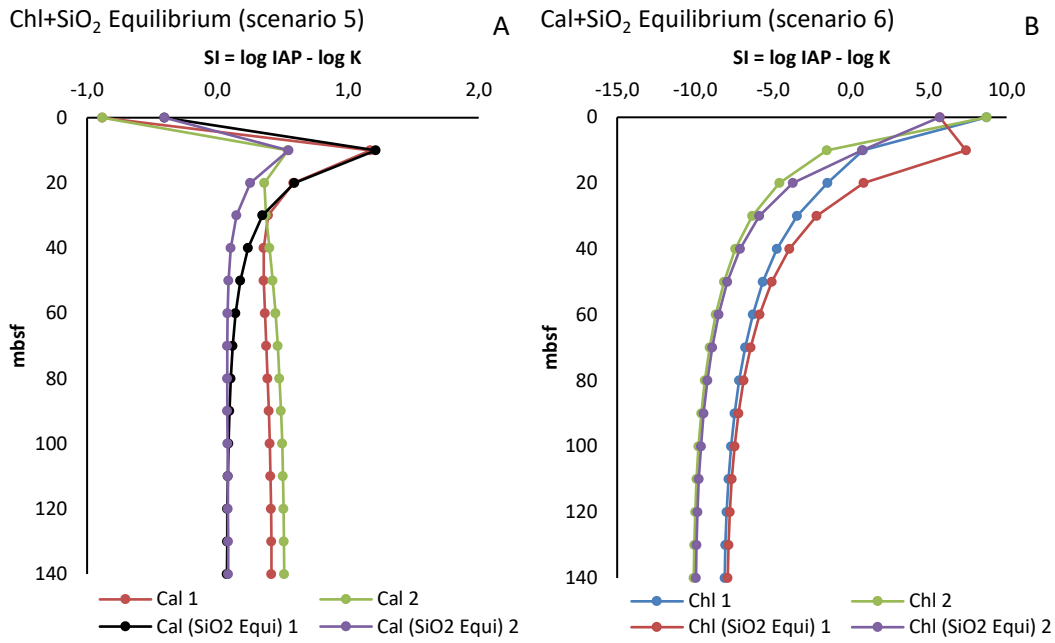

Figure 17: A: SI of calcite (Cal 1, 2) in final solution after equilibrium with chlorite + SiO_2(a) (scenario 5) and B: SI of chlorite after equilibrium of with calcite +SiO_2(a) (scenario 6). For comparison the figure shows the SI of chlorite and calcite in the case of just SiO_2(a)-equilibrium (Cal (SiO2 Equi) 1, 2 and Chl (SiO2 Equi) 1, 2) with the initial solution. The numbers 1 and 2 indicates if the input-parameter for the initial solution were taken from RT-model 1 or 2.

In general, the solution with input-parameters of RT-model 2 shows increased acidification with respect to input-parameters from RT-model 1. With respect to the equilibrium between the initial solution and SiO_2(a) the calcite oversaturation increases if chlorite is added as additional reactive phase. The undersaturation of chlorite in the initial solution (figure 14) leads to dissolution of the mineral and therefore the alkalinity of the solution increase, which causes a SI_{Cal} rise. The equilibrium of calcite with the solution strongly depends on pH and does not significant affect chlorite saturation, especially between 40 and 140 mbsf.

Figure 18 shows (1) the different amounts of precipitated/dissolved minerals of single- and multi-phase reactions depending on the input-parameters of the initial solution and (2) the influence of the scenarios 5, 6 and 21 on final pH.

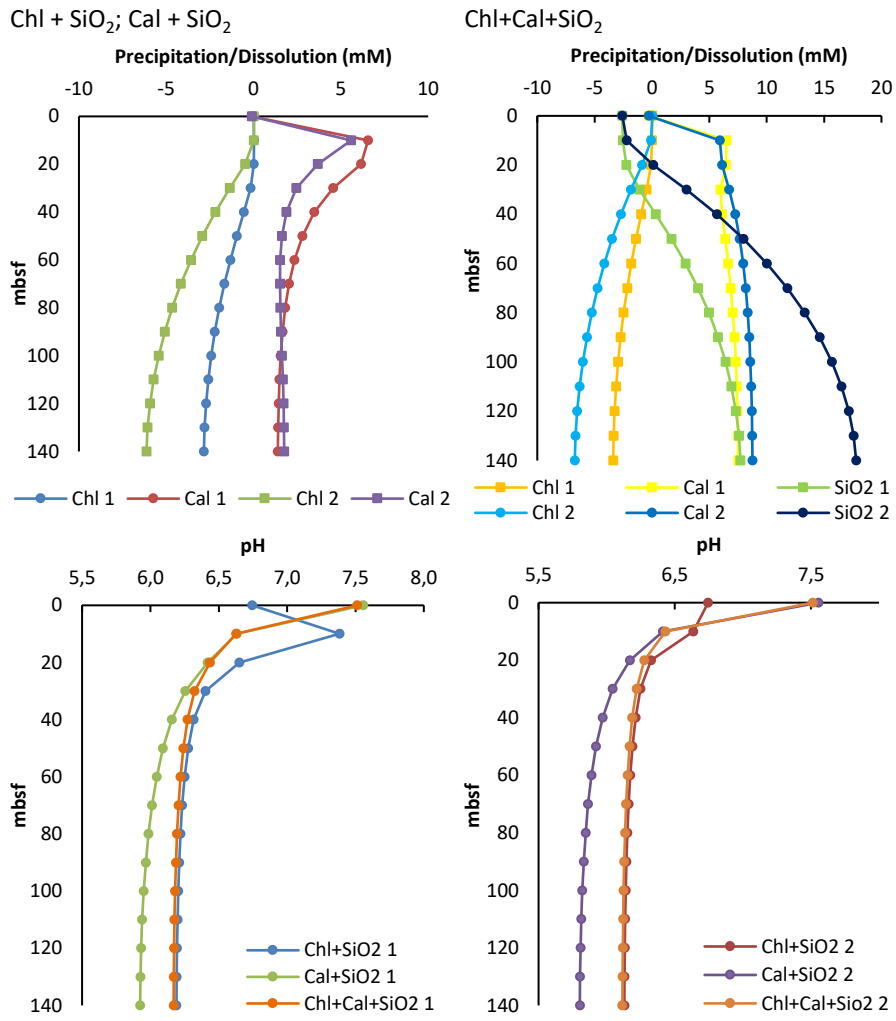

Figure: 18: Quantity of precipitated or dissoluted minerals and pH of final solution after equilibrium with initial solution in the case of chlorite +SiO_2(a) (Chl 1, 2; scenario 5), calcite + SiO_2(a) (Cal 1, 2; scenario 6) and chlorite, calcite + SiO_2(a) (Chl 1, 2; Cal 1, 2; SiO2 1, 2; scenario 21). The numbers 1 and 2 indicates if the input-parameters for the initial solution were taken from RT-model 1 or 2.

Only scenario 21 with input-parameters from RT-model 1 really produces alkalinity almost equal to the measured alkalinity of Site 1230 by the dissolution of up to 3.5 mmol/l chlorite and precipitation of up to 7.5 mmol/l calcite (figure 13; table 11). The quantity together with the stoichiometry of reacting minerals may limit maximum alkalinity of the porewater under conditions at Site 1230.

Decreasing pH leads to increasing chlorite dissolution which produces alkalinity and increases the supersaturation of calcite. Precipitation of calcite (due to the oversaturation) consumes less alkalinity than it is released by chlorite dissolution. So, the simultaneous equilibrium of chlorite and calcite + SiO_2(a) with the initial solution is characterised by higher quantities of reacted phases compared with single mineral reactions.

The contribution of theoretically +16 mol alkalinity per 1 mol dissolute chlorite (the precipitation of 1 mol calcite consumes 1 mol alkalinity) seems to control the final pH of the solution. Therefore,

final pH of scenario 21 (chlorite, calcite + SiO_2(a)) comes close to the final pH of scenario 5 (chlorite + SiO_2(a)), the opposite to the equilibrium of calcite + SiO_2(a).

Scenario 6 (with increased DIC) does not buffer lower pH-values whereas the system does not fall below a pH = 6.1 if chlorite (scenario 5 and 21) also reacts. However, the quantity of reacting chlorite depends on initial conditions. So, increasing alkalinity by cation release in scenario 21 (figure 13) together with increasing DIC in the porewater stabilises pH or vice versa: mineral solubility strongly depends on initial pH and porewater composition, the lower the initial pH the more $[H^+]$ is used (in the case of congruent dissolution) which buffers final pH.

Scenarios 5, 6 and 21 do not consider any silicate phase containing species other than MgO, CaO, Al_2O_3, SiO_2(a) and H_2O but especial the first 60 mbsf of measured $[K^+]$ profile (figure 13) indicates a K-source. Dissolution of K-feldspar, illite and montmorillonite may explain the increase in $[K^+]$ but corresponding scenarios (table 10, figure 12) do not fit $[Mg^{2+}]$, $[Ca^{2+}]$ and alkalinity of the porewater. However, in ODP Site 1230 the chlorite of scenario 21 vicariously stands for any clay mineral or silicate phase which releases cations (respectively alkalinity) due to dissolution under high DIC conditions and increased microbial activity. The deeper $[K^+]$-profile from 60 to 140 mbsf changes to a linear slope which exclude the reaction of K-bearing mineral phases K-feldspar, illite and montmorillonite.

Increasing alkalinity caused by clay-mineral equilibrium reactions cannot fully buffer the pH decrease with depth due to increasing DIC (figure 12).

Unlike the K^+ which may be released by any silicate phase for which chlorite from the model stands for, the reactions of scenario 21 (chlorite, calcite + SiO_2(a)) leads to an unmeasured enrichment of $[Al^{3+}]$ in the final solution (figure 19). This increased $[Al^{3+}]$ results from chlorite dissolution, and therefore from pH. However, the assumption of a downcore increasing $[Al^{3+}]$ in Site 1230 may lead to silicate (respectively clay mineral) and metal-(hydr)oxide precipitation, because these processes are strongly limited by aluminum concentration of the porewater.

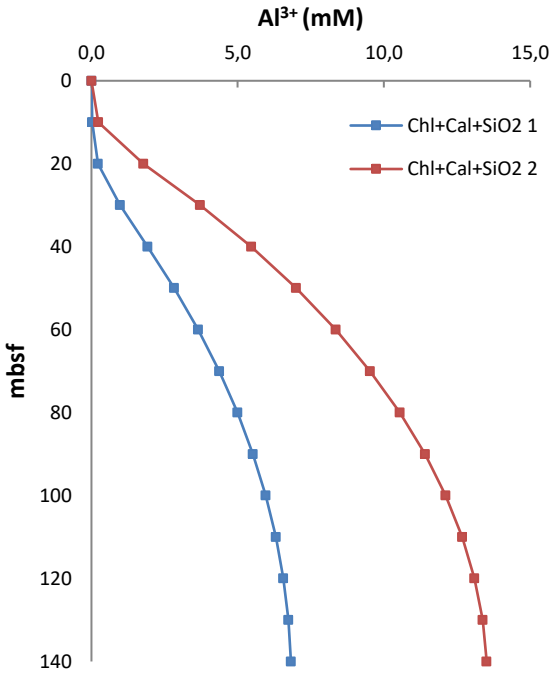

Figure 19: $[Al^{3+}]$ of final solution after equilibrium of chlorite, calcite + SiO_2(a) (Chl+Cal+SiO2 1, 2; scenario 21). The numbers 1 and 2 indicates if the input-parameter for the initial solution were taken from RT-model 1 or 2.

If only chlorite dissolves, and no other silicate mineral precipitates, the porewater becomes enriched in Al^{3+}. So it is Al^{3+} that may prevent further dissolution. This is a rather unrealistic scenario, because it is probably Al^{3+} alone that controls the mineral reaction. At least one additional phase which takes up aluminum (e.g a smectite-group mineral) may decrease [Al^{3+}] through precipitation.

Despite the absence of K_2O species in minerals of scenario 5, 6 and 21 and the Al-enrichment of final solution, the scenarios fit measured cation concentrations and alkalinity of ODP Site 1230 best. All other scenarios show very different thermodynamic behavior. In contrast to chlorite, the Al-bearing phase kaolinite is supersaturated in a solution with input-parameters from RT-model 1 and 2, which would lead to precipitation and consumption of alkalinity. The opposite behavior of kaolinite (related to chlorite) in all scenarios of Site 1230 (60-140 mbsf) may exclude scenarios (table 10) which contain kaolinite as reactive phase.

Silica and cation release through feldspar dissolution, well known under the term silicate weathering/alteration (*Wallmann et al., 2008*), produce alkalinity, but calculated scenarios do not fit measured cation concentrations of Site 1230. Scenario 1, respectively the equilibrium of K-feldspar with solution leads to the dissolution of maximum 0.05 mmol/l of feldspar, which is far too low for an influence on alkalinity. So the reaction needs additional minerals in equilibrium (e.g scenario 23) to rise its solubility, but that would enormously increase the concentration of K^+ and Mg^{2+} in porewater. If another mineral phase (e.g a smectite-group mineral) takes up Al^{3+} feldspar may show an increased reactivity. *Wallmann et al. (2008)* show that a high content of dissolved inorganic carbon in deeper methanigenic sediments promotes incongruent dissolution, which leads to an increase in porewater alkalinity. The geochemical model confirms the Al^{3+} increase in porewater through silicate dissolution, although it is unrealistic for natural systems.

5.5 Factors controlling calcite precipitation at Site 1230

In addition to measured dolomite layers in shallow depths of ODP Site 1230 (*Meister et al., 2006)*, bulk XRD analysis shows the occurrence of calcite deep in the zone of methanogenesis (figure 2B). Alkalinity production through SR and AOM in the shallow sediment and ammonium release in the deeper methanogenic zone estimated with RT-model 1 and 2 causes the slight oversaturation of calcite through the whole profile. This theoretically allows carbonate precipitation without the buffering effects of clay minerals, but precipitation is largely limited by the availability of calcium. A constant temperature of 10°C was assumed rather than a more realistic gradient. For Site 1230 a mudline-temperature of 1.7°C and 11.2°C in 278 mbsf were measured (*D'Hondt et al.,*

2003). Furthermore, a constant pressure of 500 bar in a depth of 5068 m was taken into the model. The increase in DIC is buffered by simultaneous microbial alkalinity production due to NH_4^+-release, despite large amounts of CO_2 produced by methanogenesis.

Above a depth of 30 mbsf the initial solution is characterised by an increased SI of all mineral phases K-feldspar, illite , kaolinite, montmorillonite, chlorite, calcite and SiO_2(a) (figure 14), whereas the porewater of the deeper sediment shows undersaturation of chlorite and a decrease in the $SI_{Calcite}$. The equilibrium of a solution with mineral phases strongly depends on the input-parameters DIC and alkalinity. In general, the SI follows the ratio of alkalinity and DIC calculated in Site 1230 porewater with the RT-model 1 and 2 (figure 14, table 9). Assumed initial seawater for the mineral equilibrium reactions shows a DIC/alkalinity ratio ($R_{DIC/alkalinity}$) of about 1 and changes due to more rapid increase of DIC in the deeper zone of methanogenesis (table 9).

Calcite precipitation under such conditions may need a certain ratio of DIC and alkalinity production ($R_{DIC/ALK} > 1.2$ for Site 1230), which may be favoured by (clay) mineral equilibrium reactions (figure 15). So, the key to understanding calcite precipitation under low-pH and high-alkalinity conditions at Site 1230 is the understanding of the system's mineral equilibria.

Below ≈ 15 mbsf the Ca-profile shows a constant $[Ca^{2+}]$ concentration of ≈ 4 mmol/l in porewater (figure 13). Shallow dolomite layers associated with rapidly deposited organic carbon-rich sediments along continental margins (*Pisciotto and Mahoney, 1981*) may decrease the calcium content of the porewater. Because no input of Ca^{2+} from deeper fluids occurs above 140 mbsf, calcite formation depends on the diffusion of Ca^{2+} from seawater. Carbonate precipitation in Site 1230 seems to be favoured at a depth of 60-70 mbsf due to high microbial production of alkalinity, although alkalinity release and oversaturation of calcite is highest at ≈ 10 mbsf.

There are three possible approaches to explain the occurrence of calcite between 60 and 140 mbsf: (1) authigenic calcite precipitation within the 80 m-thick sediment column due to an altered pH and alkalinity. Above and below this interval, bulk XRD does not show calcite which may indicate a kinetic inhibition of precipitation or a true $SI_{Calcite} < 0$ (because of uncertainties of the geochemical modelling). (2) as assumed for dolomite in more shallow sediments (*Kelts and McKenzie, 1980*), calcite may nucleate at a depth of 50-60 mbsf and continue growth with additional burial (due to a Ca^{2+} limitation rather unrealistic) and (3) Calcite is sedimentary.

For a better understanding of the conditions of formation in Site 1230, further investigations on $\delta^{13}C$ and $\delta^{18}O$ composition of the calcite will be measured.

Figure 13 shows the $[Ca^{2+}]$ in final solution of scenario 6 and 21 with input-parameters from RT model 1 and 2. Both scenarios fit measured $[Ca^{2+}]$ of ODP Site 1230 well.

Calcite saturation is low due to interaction with seawater which seems to be undersaturated with respect to calcite at 5000 m depth (probably below the Calcite Compensation Depth). Higher s_{TOC} produces more alkalinity in the shallow sediment due to higher SR and AOM, which increases the precipitation of carbonate (*Moore et al., 2004*). Porewater Ca-concentration sharply decreases near the surface and stays constant below a few metres. This change in slope marks the transition from undersaturation to oversaturation of calcite in the un-equilibrated solution. The theoretical possibility of the precipitation of 1g Calcite per 1000g sediment (Eq. 16) indicates a Ca^{2+} limitation of the system.

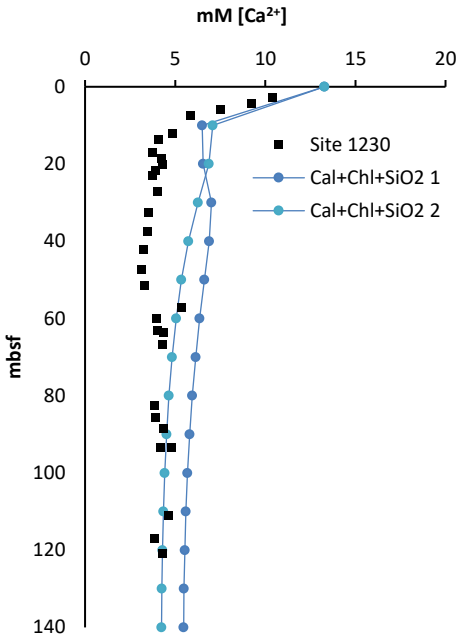

Figure 20: Calculated [Ca^{2+}] of final solution with depth after equilibrium of chlorite, calcite + SiO_2(a) (Cal+Chl+SiO2 1, 2; scenario 21). For comparison the figure also shows measured [Ca^{2+}] of ODP Site 1230. The numbers 1 and 2 indicates if the input-parameter for the initial solution were taken from RT-model 1 or 2.

A constant concentration of Ca^{2+} ≈ 4 mmol/l in final porewater shows equilibrium of calcite between sediment and porewater in Site 1230. Scenario 6 (Calcite + SiO_2(a)) equilibrium typically leads to dissolution of calcite despite increasing DIC (blue curve in figure 20) because the mineral assemblage of scenario 6 does not have the potential to buffer the resulting decrease in pH. The net effect on alkalinity of final solution through the precipitation of calcite is: alkalinity (RT-model 1) = 115 mmol/l and alkalinity (RT-model 2) = 160 mmol/l.

Opposite to that, scenario 21 allows constant calcite precipitation below 30 mbsf of Site 1230 due to a constant (respectively buffered) pH of ≈ 6.1 through chlorite dissolution (figure 18). Additional to the precipitation of up to 9 mmol/l calcite the dissolution of up to 3.5 mmol/l chlorite more than compensates the loss in alkalinity of scenario 6. The net-effect on alkalinity is an increase of ≈ 39 mmol/l with respect to the initial concentration to a final alkalinity of 154 mmol/l, which perfectly fits the measured alkalinity of Site 1230.

5.6 Limits of mineral-reaction calculations

Geochemical modelling provides a thermodynamic but non-kinetic approach on how clay mineral reactions may influence the chemistry of pore waters in anoxic deep-sea sediments. Natural systems follow the Gibbs phase rule which is described as follows:

$$F = C - P \quad \textbf{Eq. (20)}$$

where C is the number of solute concentrations which serves as model input-parameters and P is the numbers of phases in equilibrium. The concentrations of free solutes are fixed, so the number of degrees of freedom (F) is 0. Due to 7 solutes ([Ca^{2+}], [Mg^{2+}], [K^{+}], [Al^{3+}], [Si^{4+}], [DIC] and [H_2O]) the 7 defined phases (K-feldspar, illite, kaolinite, montmorillonite, chlorite, calcite and SiO_2(a)) are allowed to equilibrate. To minimise uncertainties related to this problem, the best fitting mineral combination as well as all other possible mineral combinations were calculated. In nature, there are more than 7 minerals (K-feldspar, illite, kaolinite, montmorillonite, chlorite, calcite and SiO_2(a)) in equilibrium with seawater under conditions of Site 1230, but for the model no phase other than used can be added to the presented model without violating this rule (*Gaucher et al., 2009*). The coexistence of more phases than allowed by the rule can be explained by slow reaction rates, hence, the phases do not show equilibrium.

The WATEQ-database used for calculation just includes thermodynamic data from the Mg-chlorite endmember clinochlore [$Mg_5Al_2Si_3O_{10}(OH)_8$] which may not fit the real natural occurring mineral composition. Much more realistic is a Fe-Mg chlorite with varying iron content depending on provenance. However, Fe^{x+} was not considered as input-parameter for initial solution of the geochemical model of Site 1230, so there is no Fe-bearing mineral phase.

The geochemical model considers K-feldspar, 4 clay minerals, calcite and SiO_2(a), which differ in stoichiometry, reaction-constant K and ΔH. Table 13 shows a generalised classification of possible reactions due to their H_2O and H^+ consumption/release after mineral definition in WATEQ-database. Mineral dissolution represents complete dissociation (congruent dissolution) of chemical species for calculating the speciation of a solution.

K-Fsp:	Silicate + H_2O → cations^{x+} + $Al(OH)_4^-$ + silica
Illite, (Montmorillonite):	Clay mineral + H_2O → cations^{x+} + $Al(OH)_4^-$ + silica
Kaolinite, Chlorite:	Clay mineral → cations^{x+} + silica +H_2O

Table 13: Classification of reacting minerals in geochemical model based on their dissolution stoichiometry, taken from WATEQ-database. $Al(OH)_4^-$ stands for total Al^{3+} (Σ Al^{3+}) in solution.

WATEQ-database provides two cases of clay mineral dissolution: (1) illite and montmorillonite consume H_2O whereas (2) kaolinite and chlorite show the opposite effect. Similar stoichiometry,

ΔH and K of illite and montmorillonite leads to similar results of the geochemical calculations (e.g scenario 3 and 4; figure 12). The comparison of chlorite and kaolinite shows a strong difference in thermodynamic parameters and thereby different states of saturation.

A solution showing the composition of seawater but increased DIC (respectively pH < 7) is oversaturated with kaolinite under very acidic conditions (pH ≈ 4.5) but strongly undersaturated with chlorite (figure 14). So, the equilibrium of kaolinite with the initial solution leads to precipitation of kaolinite, which consumes alkalinity through H^+ release. In opposite to chlorite dissolution, kaolinite precipitation from solution seems to be limited by low aluminum concentration if not another Al-bearing mineral (K-feldspar, illite, montmorillonite or chlorite) dissolves at the same time.

In general, geochemical modelling using the PHREEQC-code applies mineral equilibria independent of the occurrence in nature. Suggested mineral-reactions for Site 1230 are based on the best reconstruction of the measured porewater chemistry. This method does not allow conclusions on the velocity, respectively kinetics of precipitation or dissolution. However, faster kinetics may earlier lead to equilibrium conditions despite the results of the reaction model, which reaches steady state after ca. 11.2 Ma.

Finding correct thermodynamic parameters especial for clay minerals is a problem, so mineral-reactions postulate in the WATEQ-database do not necessarily represent the natural behaviour of mineral phases in anoxic sediments (*Gaucher et al., 2009*). But finding thermodynamically allowed processes while excluding impossible reactions is a great step forward in the understanding of marine sediment alteration. Clay mineral reaction-rates in deep marine sediments are very low, and even small quantities of dissolved minerals may lead to large effects in porewater alkalinity (figure 12). In addition, geochemical modelling of the porewater chemistry of Site 1230 indicates that there is no equilibrium between fluid and sediment (which is up to Eocene age).

5.7 Similarities with CO_2 storage sites

Acidification through increased pCO_2, experiments in laboratory (*Würdemann et al., 2014*) and first long-term studies of gas storage site in the northern Germanic Basin-sediments show dissolution of rock forming minerals such as feldspar, quartz and pore-filling cements (*Fischer et al., 2010*; *Kasina et al., 2014*). The comparison of anthropogenically induced mineral reactions under high pCO_2 conditions with zones of natural CO_2 production (ODP Site 1230) may help to understand long-term behavior of reservoir rock under high pCO_2 and will lead to a better understanding of sediment diagenesis.

The saturation-state of minerals strongly depends on the composition of the solution respectively porewater in natural systems. Especially the solubility of silicates and carbonates increases with CO_2-input (figure 8). CO_2-storage sites seem to be characterised by an enrichment of at least the major cations [K^+], [Mg^{2+}] and [Ca^{2+}] in porewater due to dissolution of feldspar, carbonates and clay minerals (*Wandrei et al., 2011*).

Of course, these mineral reactions are observed at 40°C (*Wandrei et al., 2011*) but also geochemical modelling of "cold" porewater-chemistry of ODP Site 1230 shows dissolution or precipitation depending on the calculated scenario. The major difference between zones of natural CO_2 production and CO_2-storage-sites is the higher alkalinity in porewater from Site 1230 generated from microbial activity and (clay) mineral reactions, which have already partially equilibrated with the mineral phases. This high alkalinity of natural sites buffers the low pH through methanogenesis, which leads to decreased quantities of reacting minerals.

The calculated maximum dissolution of 3.34 mmol/l chlorite in scenario 21 (table 11), which fits measured porewater concentration of Site 1230 best, does not affect a strong enrichment in porewater cation concentration (figure 12). More acidic conditions would automatically increase the solubility of silicates and that leads to dissolution of undersaturated mineral phases.

The difference in alkalinity between CO_2 storage sites and Site 1230 necessarily leads to an opposite observation in terms of the carbonate system. Strong acidic conditions lead to dissolution of the carbonate phases calcite and dolomite while buffered systems (such as previously described) at least theoretically allow carbonate precipitation even deep in the zone of methanogenesis. The question remains if it is possible to change the geochemical conditions of CO_2 storage sites as far to precipitate CO_2 in the form of carbonate minerals.

Microbial activity which affects the dissolution rates of feldspar, calcite, Fe(II)-minerals and sulphides, may play an important role for answering this question. The observed bacterial community in the sediments of the North German Basin adapt to changing conditions through CO_2-injectment but they do not buffer low pH (*Wandrei et al., 2016*). The influence of microbial activity in gas storage test sites and deep-sea organic carbon-rich sediments is poorly understood. An interdisciplinary approach of geology, biology and chemistry is necessary to understand mineral equilibria and geochemical modelling provides a very good method for simulation subsurface reactions between solid phases and porewater.

6. Conclusion

SO_4^{2-}, CH_4 and NH_4^+ diffusion-calculations of the porewater composition of ODP Site 1230 which considers a microbial TOC-degradation rate (s_{TOC}) of 0.001 mmol/l/a (RT-model 1), fits best measured concentrations. For comparison, a second RT-model with a s_{TOC} = 0.0017 mmol/l/a fits perfectly measured porewater alkalinity but it does not reproduce methane and ammonium concentrations.

The RT-models show that microbial activity for itself causes high concentrations of up to 115 mmol alkalinity in the porewater. Sulphate reduction and AOM in the upper part of the profile produces a significant excess of alkalinity as opposed to the deeper methanogenic zone. New is that remineralisation of NH_4^+ from organic matter degradation produces significant alkalinity within the methanogenic zone, preventing strong undersaturation and dissolution of carbonates. This high alkalinity buffers acidification caused by increased DIC (up to 240 mmol/l), and even leads to slight oversaturation of calcite between 30 and 140 mbsf of the sediment column. Mineral equilibrium reactions may provide the source for the missing 40 mmol/l alkalinity to reach measured 154 mmol/l alkalinity of porewater of ODP Site 1230.

3 scenarios (5, 6 and 21) out of 48 possible combinations of K-feldspar, illite, kaolinite, montmorillonite, chlorite, calcite + SiO_2(a) equilibria nearly reproduce measured Mg^{2+}, Ca^{2+}, K^+, DIC and alkalinity concentrations. The congruent dissolution of 2.8 mmol/l chlorite (scenario 5) leads to 160 mmol/l alkalinity in final solution which comes very close the measured value of 155 mmol/l in porewater. Due to uncertainties of input-parameters (e.g temperature, pressure and results from RT-model) and the difference between the geochemical behavior of minerals in the WATEQ-database and nature, chlorite may be exemplary for any reactive clay mineral phase under conditions of ODP Site 1230.

Calcite + SiO_2(a) (scenario 6) equilibrium with initial solution leads to small amounts of up to 2 mmol calcite precipitation which consumes an equivalent quantity of alkalinity. The depletion of [Ca^{2+}] of the porewater and calcite measured with XRD-Analysis between 60 and 140 mbsf of the profile, indicates calcite precipitation in Site 1230. Theoretical possible carbonate oversaturation in such zones of high natural DIC production potentially confirms calcite precipitation as CO_2-sink in anthropogenic CO_2-storage sites.

The equilibrium-reaction of calcite, chlorite + SiO_2(a) with porewater leads to the dissolution of up to 3.34 mmol/l chlorite and precipitation of 7.23 mmol/l calcite (table 11) which increases initial alkalinity of 115 mmol/l by up to 40 mmol/l alkalinity. So, this reaction leads to a final alkalinity of up to 155 mmol/l in final solution and reproduce best measured 154 mmol/l alkalinity and [Ca^{2+}]

from porewater of Site 1230. All other thermodynamic possible combinations of observed minerals show (1) wrong cation concentrations of final solution and/or (2) wrong alkalinity with respect to the measured 154 mmol/l alkalinity. The modelling primarily shows that thermodynamically, clay minerals have an enormous capacity to buffer acidification, but apparently they have not significantly reacted even over millions of years. This has great implications for understanding diagenetic systems but also CO_2 storage sites. It is the question whether mineral reaction kinetics is faster if pure CO_2 (without alkalinity from microbial activity) is added.

7. Acknowledgments

Great Thanks to Patrick Meister for breaking the spell of the “calcite witch” and Susanne Gier for her help for a better understanding of clay mineral reactions. In addition, thanks to all colleagues and friends who contributes to the work with lively discussions.

8. References

Aloisi, G., Wallmann, K., Drews, M., Bohrmann, G., 2004. Evidence for the submarine weathering of silicate minerals in Black Sea sediments: possible implications for the marine Li and B cycles. Geochem. Geophys. Geosyst. 5, Q04007.

Amiotte Suchet, P., Probst, J.L., Ludwig, W., 2003. Worldwide distribution of continental rock lithology: Implications for the atmospheric/soil CO_2 uptake by continental weathering and alkalinity river transport to the oceans, Global Biogeochem. Cycles, 17, 1038–1051.

Arndt, S., Brumsack, H.J., Wirtz, K.W., 2006. Cretaceous black shales as active bioreactors: a biogeochemical model for the deep biosphere encountered during ODP Leg 207 (Demarara Rise), Geochim. Cosmochim. Acta 70, 408–425.

Arndt, S., Hetzel, A., Brumsack, H.J., 2009. Evolution of organic matter degradation in Cretaceous black shales inferred from authigenic barite: a reaction-transport model. Geochim. Cosmochim. Acta 73, 2000–2022.

Arndt, S., Jørgensen, B.B., LaRowe, D.E., Middelburg, J.J., Pancost, R.D., Regnier, P., 2013. Quantifying the degradation of organic matter in marine sediments: A review and synthesis, Earth-Science Reviews 123, 53–86, Elsevier B.V., Amsterdam.

Arning, E.T., van Berk, W., Schulz, H.M., 2012. Quantitative geochemical modeling along a transect off Peru: Carbon cycling in time and space, and the triggering factors for carbon loss and storage, Global Biogeochem. Cycles, 26, GB4012, doi:10.1029/2011GB004156.

Boudreau, B.P. 1997. Diagenetic models and their implementation: modelling transport and reactions in aquatic sediments. Springer, Berlin, Heidelberg, New York.

Bruland, K.W., Lohan, M.C., 2004. Controls of Trace Metals in Seawater. In: Treatise on Geochemistry. Holland, H.D. and Turekian, K.K. (Editors), Elsevier B.V., Amsterdam. 6: 23-47.

Broecker K.W., Peng T.H., 1982. Tracers in the Sea. Eldigo Press, Palisades, NY.

Colbourn, G., Ridgwell, A., Lenton, T.M. 2015. The time scale of the silicate weathering negative feedback on atmospheric CO2. Global Biogeochemical Cycles, 29(5), 583–596 . DOI: 10.1002/2014GB005054

Deer, W.A., Howre, R.A., Zussman, J. 1963. Rock forming minerals, Vol 4, Framework silicates, John Wiley and Sons, New York.

D'Hondt, S.D., Rutherford, S., Spivack, A.J., 2002. Metabolic activity of the subsurface biosphere in deep-sea sediments. Science, 295:2067–2070.

D'Hondt, S.L., Jørgensen, B.B., Miller, D.J., et al., 2003. Proc. ODP, Init. Repts., 201 [CD-ROM]. Available from: Ocean Drilling Program, Texas A&M University, College Station TX 77845-9547, USA.

Donohue, C.M., Snyder, G.T., Dickens, G.R., 2006. Data report: Major cation concentrations of interstitial waters collected from deep sediments of eastern equatorial Pacific and Peru Margin (ODP Leg 201), *in* Jørgensen, B.B., et al., eds., Proceedings of the Ocean Drilling Program, Scientific results, Volume 201: College Station, Texas, Ocean Drilling Program, p. 1–19, doi:10.2973/odp.proc.sr.201.104.2006.

Engelhardt, W., Füchtbauer, H., Müller, G., 1974. Sedimentary Petrology: Methods In Sedimentary Petrology, Volume 1, Schweizerbart.

Eslinger, E., Pevear, D.R., 1988. Clay minerals and Sandstone diagenesis. Clay minerals for petroleum geologists and engeneers. SEPM Short Course 22, 6.1-6.29.

Fischer, S., Liebscher, A., Wandrey M., 2010. CO_2-brine-rock interactions – First results of long-term exposure experiments at in situ p-T conditions of the Ketzin CO_2 reservoir. Chemie der Erde 70, S3, 155-164, Elsevier B.V., doi:10.1016/j.chemer.2010.06.001.

Fischer, S., Szizybalski, A., Zimmer, M., Kujawa, C., Plessen, B., Liebscher, A., Moeller, F., 2014. N_2-CO_2 coinjection field test at the Ketzin pilot CO2 storage site. Energy Procedia 63, 2848-2854, Elsevier B.V., Amsterdam, doi: 10.1016/j.egypro.2014.11.307.

Froelich, P.N., Klinkhammer, G.P., Bender, M.L., Luedtke, N.A., Heath, G.R., Cullen, D., Dauphin, P., Hammond, D., Hartman, B., Maynard, V., 1979. Early oxidation of organic matter in pelagic sediments of the eastern equatorial Atlantic: suboxic diagenesis. Geochim. Cosmochim. Acta 43 (7), 1075–1090.

Gaucher, E., Robelin, C., Matray, J. M., Negrel, G., Gros, Y., Heitz, J.F., Vinsot, A., Rebours, H., Cassabagnere, A., Bouchet A., 2004. ANDRA underground research laboratory: interpretation of the mineralogical and geochemical data acquired in the Callovian-Oxfordian Formation by investigative drilling. Phys. Chem. Earth 29, 55–77.

Gaucher, E.C., Tournassat, C., Pearson, F.J., Blanc, P., Crouzet C., Lerouge, C., Altmann, S., 2009. A robust model for pore-water chemistry of clayrock. Geochim. Cosmochim. Acta, 0016-7037, doi:10.1016/j.gca.2009.07.021.

Heini, K., Rajala, P., Carpen, L., Bomberg, M., 2015. Nitrate and ammonia as nitrogen sources for deep subsurface microorganisms. Front. Microbiol. 6:1079. doi: 10.3389/fmicb.2015.01079.

Hussong, D.M., Wipperman, L.K., 1981. Vertical movement and tectonic erosion of the continental wall of the Peru-Chile Trench near 11°30'S latitude. In Kulm, L. D., Dymond, J., Dasch, E. J., and Hussong, D. M. (Eds.), Nazca Plate: Crustal Formation and Andean Convergence. Geol. Soc. Am. Mem., 154:504-524.

Hussong, D.M., Dang, S. P., Kulm, L.D., Couch, R.W., Hilde, T.W.C. (Eds.), 1985a. Atlas of the Ocean Margin Program, Peru Continental Margin, Region VI: Woods Hole (Marine Science International).

Jasmund, K, Lagaly, G., 1993. Tonminerale und Tone: Struktur, Eigenschaften, Anwendungen und Einsatz in Industrie und Umwelt. Darmstadt: Steinkopff, ISBN 3-7985-0923-9.

Kasina, M., Morozova, D., Michalik, M., Pudlo, D., Würdemann, H., 2014. Impact of gas storage on reservoir rocks – long-term study to investigate the effects on mineral content and fluid chemistry. Energy Procedia 59, 418-424, Elsevier B.V., Amsterdam, doi: 10.1016/j.egypro.2014.10.397.

Kastner, M., Elderfield, H., Martin, J.B., Suess, E., Kvenvolden, K.A., Garrison, R.E., 1990. Diagenesis and interstitial-water chemistry at the Peruvian Continental Margin, major constituents and strontium isotopes. In: Suess, E., von Huene (Eds.), Proc ODP, Sci Results, v. 112. Ocean Drilling Program, College Station, TX, pp. 413–440.

Kelts, K.R., and McKenzie, J.A., 1980. Formation of deep-sea dolomite in anoxic diatomaceous oozes. Twenty-sixth Internatl. Geol. Congr., Paris, France. (Abstract).

Konhauser, K., 2006. Introduction to Geomicrobiology. Wiley-Blackwell, New York.

Kulm, L.D., Dymond, J., Dasch, E.J., Hussong, D.M. (Eds.), 1981. Nazca Plate: Crustal Formation and Andean Convergence. Geol. Soc. Am. Mem., 154.

Kulm, L.D., Suess, E., Thornburg, T.M., 1984. Dolomites in the organic-rich muds of the Peru fore-arc basins: Analogue to the Monterey Formation. In Garrison, R. E., Kastner, M., and Zenger, D. (Eds.), Dolomites in the Monterey Formation and other Organic-rich Units. Soc. Econ. Paleontol. Min. Spec. Publ., 41:29-48.

Lumsden, D.N., Morrison, J.W, Lioyd, R.V., 1995. The Role of Iron and Mg/Ca Ratio in Dolomite Synthesis at 192°C1. The Journal of Geology, Vol. 103, No. 1, pp. 51-61.

Marion, G.M., Millero F.J.B., Camoes M.F., Spitzer P., Feistel R. Chen C.T.A., 2011. pH of seawater. Mar. Chem. 126, 89–96.

Meister, P., McKenzie, J.A., Warthmann, R., and Vasconcelos, C., 2006. Mineralogy and petrography of diagenetic dolomite, Peru margin, ODP Leg 201. In Jørgensen, B.B., D'Hondt, S.L., and Miller, D.J. (Eds.), Proc. ODP, Sci. Results, 201, 1–34 [Online].

Meister, P., McKenzie, J.A., Vasconcelos, C., Bernasconi, S., Frank, M., Gutjahr, M., Schrag, D.P., 2007. Dolomite formation in the dynamic deep biosphere. Sedimentology 54, 1007-1032.

Meister, P., Gutjahr, M., Frank, M., Bernasconi, S., Vasconcelos, C., McKenzie, J., 2011. Dolomite formation within the methanogenic zone induced by tectonically driven fluids in the Peru accretionary prism. Geology 39, 563–566.

Meister, P., Liu, B., Ferdelman, T.G., Jørgensen, B.B., and Khalili, A. 2013. Control of sulphate and methane distributions in marine sediments by organic matter reactivity. *Geochim. Cosmochim. Acta*. 104, 183-193.

Merkel, B.J, Nordstrom, D.K, Planer-Friedrich, B., 2008. Groundwater Geochemistry: A Practical Guide to Modeling of Natural and Contaminated Aquatic Systems. Berlin [u.a.]: Springer ISBN 978-3-540-74667-6.

Michalopoulos, P., Aller R.C., 1995. Rapid clay mineral formation in Amazon delta sediments: reverse weathering and oceanic element cycles. Science 270, 614–616.

Moore, D.M., Reynolds, R.C., 1997. X-Ray Diffraction and the Identification and Analysis of Clay Minerals, 2nd ed. Oxford, New York: Oxford University Press.

Moore, T.S., Murray, R.W., Kurtz, A.C., Schrag, D.P., 2004. Anaerobic methane oxidation and the formation of dolomite. Earth and Planetary Science Letters 229, 141– 154. Elsevier B.V., Amsterdam.

Norrish, K., Taylor R.M. 1962. Quantitative Analysis by X-Ray Diffraction. Division of Soils, C.S.I.R.O., Adelaid, South Australia.

Parkes, R.J., Webster, G., Cragg, B.A., Weightman, A.J., Newberry, C.J., Ferdelman, T. G., Kallmeyer, J., Jørgensen, B.B., Aiello, I.W., Fry, J.C., 2005. Deep sub-seafloor prokaryotes simulated at interfaces over geological time. Nature 436, 390–394. 1816.

Parkhurst, D., Appelo C., 1999. A user´s U.S. Geological guide to Survey, PHREEQC (version 2) - A computer program for speciation, batch - reaction, one - dimensional transport and inverse geochemical calculations: Denver Colorado. pp. 1–312.

Parkhurst, D., Appelo C., 2013. Description of Input and Examples for PHREEQC Version 3—A Computer Program for Speciation, Batch-Reaction, One-Dimensional Transport, and Inverse Geochemical Calculations. U.S. Geological Survey Techniques and Methods.

Pisciotto, K.H., Mahoney, J.J., 1981. Isotopic Survey Of Diagenetic Carbonates, Deep Sea Drilling Project Leg 63. Initial Reports of the Deep Sea Drilling Project, Volume 6.

Prokopenko, M. G., Hammond, D. E., Spivack, A. J.; Stott, L. D. 2006. Sediment and pore water C and N composition of ODP Holes 201-1227A and 201-1230A. doi:10.1594/PANGAEA.773410.

Schmidt, C., Behrens, S., Kappler, A., 2011. Ecosystem functioning from a geomicrobiological perspective – a conceptual framework for biogeochemical iron cycling. Environ. Chem. 7, 399–405.

Scholz, F., Hensen, C., Schmidt, M., Geersen, J., 2013. Submarine weathering of silicate minerals and the extent of pore water freshening at active continental margins. Geochim. et Cosmocim. Acta 100, 200-216. Elsevier B.V., Amsterdam.

Schulz, H.D., Zabel, M., 2006. Marine Geochemistry. 2nd Edition, Springer Verlag, Heidelberg, NY.

Spivack, A.J., McNeil, C., Holm, N.G., Hinrichs, K.-U., 2006. Determination of in situ methane based on analysis of void gas. In Jørgensen, B.B., D'Hondt, S.L., and Miller, D.J. (Eds.), Proc. ODP, Sci. Results, 201, 1–11.

Tucker, M., 2017. Techniques in sedimentology. edited by Maurice Tucker. SERBIULA (sistema Librum 2.0).

Wallmann, K., Aloisi, G., Haeckel, M., Tishchenko, P., Pavlova, G., Greinert, J., Kutterolf, S., Eisenhauer, A., 2008. Silicate weathering in anoxic marine sediments. Geochim. Cosmochim. Acta 72, 3067–3090. Elsevier B.V., Amsterdam.

Wehrmann, L.M., Ockert, C., Mix, A.C., Gussone, N., Teichert, B.M.A., Meister, P., 2013. Repeated occurrences of methanogenic zones, diagenetic dolomite formation and linked silicate alteration in southern Bering Sea sediments (Bowers Ridge, IODP Exp. 323 Site U1341). Deep-Sea Research II. Elsevier B.V., Amsterdam, doi.org/10.1016/j.dsr2.2013.09.008.

Wandrey, M., Fischer, S., Zemke, k., Liebscher, A., Scherf, A.K., Vieth-Hillebrand, A., Zettlitzer, M., Würdemann, H., 2011. Monitoring petrophysical, mineralogical, geochemical and microbiological effects of CO_2 exposure - Results of long-term experiments under in situ conditions. Energy Procedia 4, 3644-3650, Elsevier B.V., doi:10.1016/j.egypro.2011.02.295.

9. Appendix

Alkalinity of final solution (mM)						
	RT Model 1			RT Model 2		
mbsf	Scenario 5 Chl+SiO_2	Scenario 6 Cal+SiO_2	Scenario 21 Chl+Cal+SiO_2	Scenario 5 Chl+SiO_2	Scenario 6 Cal+SiO_2	Scenario 21 Chl+Cal+SiO_2
SW	1.7	2.3	2.3	1.7	2.3	2.3
10	48.5	35.8	35.7	63.5	52.6	53.3
20	68.5	56.4	57.2	90.8	75.7	84.7
30	79.5	67.8	72.3	118.1	91.4	112.2
40	92.2	76.4	86.2	143.3	104.5	137.1
50	104.5	83.7	98.8	166.0	115.8	159.4
60	115.8	89.9	110.1	186.2	125.7	179.4
70	125.9	95.1	120.0	204.0	134.4	196.9
80	134.7	99.6	128.7	219.5	141.8	212.2
90	142.2	103.4	136.1	232.7	148.1	225.2
100	148.5	106.5	142.3	243.7	153.3	236.0
110	153.4	108.9	147.2	252.4	157.5	244.6
120	157.2	110.7	150.8	258.9	160.6	251.1
130	159.6	112.0	153.3	263.3	162.7	255.4
140	160.9	112.6	154.5	265.5	163.7	257.5

Appendix 1: Alkalinity calculated wit RT-model for scenario 5, 6 and 21

	RT Model 1					RT Model 2				
mbsf	SO_4^{2-} mM	CH_4 mM	NH_4^+ mM	DIC mM	Alkalinity mM	SO_4^{2-} mM	CH_4 mM	NH_4^+ mM	DIC mM	Alkalinity mM
SW	28.00	0.00	0.00	2.00	2.10	28.00	0.00	0.00	2.00	2.10
10	7.13	7.38	5.17	49.97	48.94	3.17	19.36	8.80	73.86	62.34
20	0.60	22.46	9.98	82.60	68.71	0.13	50.12	16.96	122.03	81.36
30	0.03	39.86	14.41	107.61	76.87	0.00	80.23	24.50	163.90	93.91
40	0.00	56.12	18.47	130.03	83.41	0.00	107.88	31.40	202.08	105.16
50	0.00	70.92	22.16	150.33	89.28	0.00	133.01	37.68	236.70	115.35
60	0.00	84.22	25.49	168.55	94.54	0.00	155.62	43.32	267.78	124.49
70	0.00	96.05	28.44	184.71	99.19	0.00	175.70	48.34	295.36	132.59
80	0.00	106.39	31.02	198.82	103.25	0.00	193.26	52.73	319.44	139.66
90	0.00	115.25	33.23	210.90	106.72	0.00	208.31	56.50	340.04	145.70
100	0.00	122.63	35.08	220.95	109.60	0.00	220.85	59.63	357.19	150.73
110	0.00	128.53	36.55	228.98	111.90	0.00	230.88	62.14	370.89	154.74
120	0.00	132.96	37.66	234.99	113.62	0.00	238.40	64.02	381.15	157.74
130	0.00	135.91	38.40	239.00	114.77	0.00	243.41	65.28	387.99	159.74
140	0.00	137.39	38.77	241.00	115.34	0.00	245.92	65.90	391.41	160.74

Appendix 2: Cation-, DIC and alkalinity concentrations calculated with the RT-model

Abstract (german)

Die CO_3^{2-}-Sättigung im Porenwasser mariner Sedimente bestimmt maßgeblich die Möglichkeit der authigenen Karbonatfällung. Starke mikrobielle Aktivität, insbesondere Sulphatreduktion und anaerobe Oxidation von Methan, produziert Alkalinität und begünstigt die Karbonatbildung, während Methanogenese den pH-Wert des Porenwassers, durch einen Anstieg an gelöstem CO_2 (DIC) verringert. Ohne Puffer-Effekte führt diese „Versauerung" zu einer Auflösung von Karbonaten.

Die Verwitterung von Silikaten während der frühen Diagenese scheint einen Einfluss auf die Alkalinität des Porenwassers zu haben und es wird angenommen, dass zusätzliche Alkalinität durch die Lösung untersättigter Tonminerale produziert wird. Diese Prozesse scheinen einen großen Einfluss auf die Karbonatdiagenese zu haben und könnten sogar in stark methanogenen Zonen zur Karbonatfällung führen.

Diese Studie quantifiziert den Anteil mikrobiell produzierter Alkalinität an der gemessenen Gesamtalkalinität im Porenwasser der ODP, Leg 201, Site 1230 (Ocean Drilling Project) mittels eines Diffusions-Modells. Des Weiteren wurde die Möglichkeit eines Anstieges der Alkalinität durch Gleichgewichtsreaktionen von Tonmineralen simuliert. Obwohl das Modell DIC-Konzentrationen von bis zu 240 mmol/l ergibt, bewirken 115 mmol/l mikrobiell produzierter Alkalinität, dass Calzit bis zu einer Profiltiefe von 140 mbsf leicht übersättigt ist. Die XRD-Analyse von Sedimenten der ODP Site 1230 ergab einen Calzitnachweis zwischen 60 und 140 mbsf.

Für die Berechnungen der Tonmineralgleichgewichte wurde der PHREEQC-Code, bereitgestellt vom United State Geological Survey, verwendet. 3 von 48 thermodynamisch möglichen Mineralkombinationen von K-Feldspat, Illit, Kaolinit, Montmorillonit, Chlorit, Calzit und Opal A (SiO_2) reproduzierten die im ODP Site 1230 Profil gemessenen [Ca^{2+}]-, [Mg^{2+}]-, DIC-Konzentrationen und Alkalinitätswerte am besten.

Die Ergebnisse zeigen, dass Tonminerale in Tiefseesedimenten weit weg von einem Gleichgewicht und mögliche Reaktionen kinetisch gehemmt sind. Die Überwindung dieser kinetischen Barrieren wäre unerlässlich für die ersten Konzepte von CO_2-Speicherreservoiren in geeigneten geologischen Einheiten (*Fischer et al., 2010; Kasina et al., 2014*). Die Ausfällung von Karbonaten könnte dazu führen, dass CO_2 in Form von Karbonatgestein dauerhaft gespeichert wird. Hierbei ist die geochemische Modellierung eine wichtige Methode, um komplexe Probleme in diesem Zusammenhang zu verstehen (zB *Boudreau, 1997*).